Since January 2020 Elsevier has created a COVID-19 resource centre with free information in English and Mandarin on the novel coronavirus COVID-19. The COVID-19 resource centre is hosted on Elsevier Connect, the company's public news and information website.

International Journal of Pharmaceutics 607 (2021) 121023

Contents lists available at ScienceDirect

International Journal of Pharmaceutics

journal homepage: www.elsevier.com/locate/ijpharm

Fluoxetine hydrochloride loaded lipid polymer hybrid nanoparticles showed possible efficiency against SARS-CoV-2 infection

Shaymaa Elsayed Khater [a], Ahmed El-khouly [b,c], Hend Mohamed Abdel-Bar [a,*], Abdulaziz Mohsen Al-mahallawi [d,e], Dalia Mahmoud Ghorab [d]

[a] Department of Pharmaceutics, Faculty of Pharmacy, University of Sadat City, Sadat City, Egypt
[b] Department of Organic and Medicinal Chemistry, Faculty of Pharmacy, University of Sadat City, Sadat City, Egypt
[c] Department of Pharmaceutical Sciences, Faculty of Pharmacy, Jerash University, Jerash, Jordan
[d] Department of Pharmaceutics and Industrial Pharmacy, Faculty of Pharmacy, Cairo University, Egypt
[e] School of Life and Medical Sciences, University of Hertfordshire Hosted by Global Academic Foundation, New Administrative Capital, Cairo, Egypt

ARTICLE INFO

Keywords:
COVID-19
SARS-COV-2 main protease
Drug repurposing
SSRIs
Molecular docking
Fluoxetine hydrochloride
Lipid polymer hybrid

ABSTRACT

Up to date, there were no approved drugs against coronavirus (COVID-19) disease that dangerously affects global health and the economy. Repurposing the existing drugs would be a promising approach for COVID-19 management. The antidepressant drugs, selective serotonin reuptake inhibitors (SSRIs) class, have antiviral, anti-inflammatory, and anticoagulant effects, which makes them auspicious drugs for COVID 19 treatment. Therefore, this study aimed to predict the possible therapeutic activity of SSRIs against COVID-19. Firstly, molecular docking studies were performed to hypothesize the possible interaction of SSRIs to the Severe Acute Respiratory Syndrome coronavirus 2 (SARS-COV-2) main protease. Secondly, the candidate drug was loaded in lipid polymer hybrid (LPH) nanoparticles to enhance its activity. The studied SSRIs were Fluoxetine hydrochloride (FH), Atomoxteine, Paroxetine, Nisoxteine, Repoxteine RR, and Repoxteine SS. Interestingly, FH could effectively bind with SARS-COV-2 main protease via hydrogen bond formation with low binding energy (-6.7 kcal/mol). Moreover, the optimization of FH-LPH formulation achieved 65.1 ± 2.7% encapsulation efficiency, 10.3 ± 0.4% loading efficiency, 98.5 ± 3.5 nm particle size, and −10.5 ± 0.45 mV zeta potential. Additionally, it improved cellular internalization in a time-dependent manner with good biocompatibility on Human lung fibroblast (CCD-19Lu) cells. Therefore, the study suggested the potential activity of FH-LPH nanoparticles against the COVID-19 pandemic.

1. Introduction

COVID-19 instigate severe acute respiratory syndrome caused by infection of coronavirus 2 (SARS-CoV2) (Gil et al., 2020). The ability of both symptomatic and asymptomatic cases to spread COVID-19 infection makes it a pandemic disease in just a few months (Wu et al., 2020), which has negatively affected the global economy (Udugama et al., 2020). Consequently, more efforts are needed to find new innovative approaches that could fundamentally change our understanding and management of this disaster (Nicola et al., 2020).

SARS-COV-2 consisted of a single-strand positive Ribonucleic acid (ssRNA) genome that was enveloped within a membrane and surrounded by glycoprotein spikes (S- protein) with a crown-like appearance (Liu et al., 2020). The viral cellular penetration is prompted by the interaction of the viral spike (S) glycoprotein with the angiotensin-converting enzyme 2 (ACE2) receptor (Zhou et al., 2020). Consequently, host transmembrane serine protease 2 cleaves the S protein to fuse to the host cell membrane and internalizes it via the endocytic pathway (Hoffmann et al., 2020).

Moreover, the viral genome was split by the main proteases enzymes including 3 carbon-like proteases (3CLpro) and the papain-like protease (PLpro) to yield nonstructural proteins (nsp2 – 16), which are essential for replication – transcription complex formation (V'kovski et al., 2019). Additionally, RNA-Dependent RNA Polymerase mediates the transcription and replication of the viral RNA genome through infection (Gil et al., 2020). Particularly, all SARS-CoV2 enzymes and proteins that participated in the virus life cycle could be considered as potential targets for the treatment of this crisis (Gil et al., 2020).

* Corresponding author at: Department of Pharmaceutics, Faculty of Pharmacy, University of Sadat City, Menoufia, Egypt.
E-mail address: hend.abdelbar@fop.usc.edu.eg (H.M. Abdel-Bar).

https://doi.org/10.1016/j.ijpharm.2021.121023
Received 1 June 2021; Received in revised form 5 August 2021; Accepted 15 August 2021
Available online 18 August 2021

Up to date, there was no approved drug for COVID-19 treatment, so the repurposing of approved drugs could effectively shorten the required time and decreased the cost compared to the new drug discovery (Trezza et al., 2020). Plenty of drugs have been subjected for drug repurposing to combat COVID-19 either antiviral or non-antiviral supporting agents and miscellaneous drugs (Elmezayen et al., 2020). Molecular docking is a drug design approach used to determine the interaction of essential amino acids between the targeted protein and the candidate ligands with low binding energy (Carlesso et al., 2019). Moreover, it predicts the binding affinity and the inhibition efficiency of the candidate ligand for the targeted protein (Huang et al., 2018).

The selective serotonin reuptake inhibitors (SSRIs) are considered safe and effective antidepressant drugs that are mostly prescribed worldwide for the treatment of major depressive disorder disease (Kennedy et al., 2016). Recently, several studies examined their activity against COVID-19. Firstly, an observational study reported the potential association between the administration of certain antidepressant drugs including fluoxetine, venlafaxine, paroxetine, and mirtazapine, and the decrease in risk of intubation or death in hospitalized COVID-19 patients (Hoertel et al., 2020, 2021c). And this association was confirmed by several observational studies (Diez-Quevedo et al., 2021; Hoertel et al., 2021a, 2021b). Secondly, several preclinical in-vitro studies reported the potential activity of fluoxetine alone (Dechaumes et al., 2021; Zimniak et al., 2021) or in combination with antiviral drugs on COVID-19 (Schloer et al., 2021). Finally, clinical trials suggested that the antidepressant drug, fluvoxamine, can inhibit clinical deterioration in acute COVID-19 outpatients (Lenze et al., 2020; Seftel and Boulware, 2021).

The activity of antidepressant drugs on COVID-19 may be attributed to their ability to inhibit acid sphingomyelinase enzyme which decreases the release of ceramide on the epithelial cell surface (Gulbins et al., 2013; Kölzer et al., 2004). Consequently, they can prevent the infection of epithelial cells with COVID-19 as reported by preclinical (Carpinteiro et al., 2021, 2020) and observational studies (Hoertel et al., 2021a, 2021b). Additionally, their sigma-1 receptor agonists effect (Lenze et al., 2020; Rosen et al., 2019; Roumestan et al., 2007; Wang et al., 2019) decreases the elevated cytokine level in COVID 19 patients (Gordon et al., 2020; Hojyo et al., 2020). Furthermore, they can reduce the plasma level of numerous inflammatory mediators that are associated with COVID-19 (Köhler et al., 2018; Marín-Corral et al., 2021). Finally, their anticoagulant effect (Halperin and Reber, 2007) makes them the optimum choice for COVID-19 patients who have arterial and venous thrombosis (Hamed and Hagag, 2020).

Moreover, drug loading in nanocarriers improves its therapeutic efficacy and reduces its side effects (Kumar et al., 2020). Recently, lipid polymer hybrid (LPH) nanoparticles received great attention in scientific research (Mukherjee et al., 2019). It consists of a polymeric core that is surrounded by a single or multiple layers of lipids. Besides, LPH could encapsulate hydrophilic, lipophilic, and amphiphilic drugs with good biocompatibility and easily functionalize with different targeting ligands (Jiang et al., 2020).

Therefore, this study firstly aimed to investigate the binding affinity of the SSRIs to the SARS-COV-2 main protease through the molecular docking study. Secondly, the candidate SSRIs molecule was encapsulated in LPH nanoparticles to improve its cellular uptake by the human lung fibroblast (CCD-19Lu) cells and consequently enhance its therapeutic activity against COVID-19. The selected SSRIs were Fluoxetine hydrochloride (FH), Atomoxteine, Paroxetine, Nisoxteine, Repoxteine RR, and Repoxteine SS. The prepared LPH formulations were optimized using the Box-Benken design. Moreover, the architecture and the surface morphology of the LPH dispersion were visualized by transmission electron microscope (TEM) and atomic force microscope (AFM). The biocompatibility of the optimized LPH formula was assessed using the MTT assay and the quantitative assessment of the cellular uptake was measured by the flow cytometry.

2. Materials and methods

2.1. Materials

Fluoxetine hydrochloride (FH) (M_W: 345.79) was kindly provided by Delta Pharma for the Pharmaceutical Industry, Egypt. Poly lactide co glycolic acid (PLGA) 50/50 DL-lactide/glycolide with an inherent viscosity midpoint of 0.2 dL/g was kindly supplied from Purac Biomaterials, the Netherlands. Acetonitrile (HPLC grade), Ethanol absolute, Lecithin soybean (LEC) (3-*sn*-Phosphatidylcholine $\geq$ 99% (TLC) lyophilized powder), Triethylamine, Fetal bovine serum (FBS), and Dimethylsulphoxide (DMSO) were purchased from Sigma Aldrich, USA. Hydrochloric acid, potassium chloride, potassium dihydrogen orthophosphate, sodium chloride, sodium dibasic hydrogen orthophosphate, sodium hydroxide, and Tween 80 were purchased from Fluka Chemika-BioChemika, Switzerland. Triton™ X-100, 1,1′-Dioctadecyl-3,3,3′,3′-Tetramethylindocarbocyanine Perchlorate (DiI), and 3-(4,5-dimethylthiazol-2-yl)-2,5-diphenyltetrazolium bromide (MTT) were purchased from ThermoFisher Scientific, UK. Dulbeccós Modified Eaglés Media (DMEM), L-glutamine, penicillin, streptomycin, and trypsin-EDTA were purchased from Gibco, Invitrogen, UK. Human lung fibroblast (CCD-19Lu) cells (catalog number ATCC® CCL-210™) were purchased from The American Type Culture Collection (ATCC, UK).

2.2. Methods

2.2.1. Molecular Docking Study

2.2.1.1. Molecular docking materials. Docking studies were attempted to explore the binding mode of the suggested compounds onto the three-dimensional (3D) model of the main protease of SARS-COV-2 using AUTODOCK tools version 1.5.6 available from Scripps Research Institute (Autodock) (http://autodock.scripps.edu/resources/adt). The 3D crystal structures for SARS-COV-2 main protease in complex with 2-(5-cyanopyridin-3-yl)-N-(pyridine-3-yl) acetamide (5RGW) were retrieved from PDB (https://www.rcsb.org/structure/5RGW). The ligand, water molecules, and heteroatoms were removed, polar hydrogens were added, Kollman charges were added, Gasteiger charges were calculated (Anupama et al., 2019). Furthermore, the atoms were assigned to AutoDock 4 type and consequently, the enzymes were converted to the PDBQT files using Autodock tools.

Chemical structures and the 3D conformers of the selected SSRIs were downloaded from Pubchem (https://pubchem.ncbi.nlm.nih.gov/) (**Fig. S1**) (FH (CID = 62857), Atomoxteine (CID = 54841), Paroxetine (CID = 43815), Nisoxteine hydrochloride (CID = 134453), Repoxteine RR (CID = 127150), Repoxteine SS (CID = 65856)). The energy of the 3D conformers was minimized by Avogadro (https://avogadro.cc/) using the Merck Molecular Force Field (MMFF94) and saved as a PDB file. Then its torsions were set and converted to PDBQT using AutoDock Tools.

2.2.1.2. Molecular Docking procedure. The docking simulations were carried out by AutoDock Vina (http://vina.scripps.edu/) (Allouche, 2012). Ligands centered with a spacing of 1.0 Å, size_X = 15, size_Y = 12, size_Z = 15 and center_X = − 8.433, center_y = -0.232 and center_z = 20.977. These dimensions and coordination were determined using AutoDock Tools Grid Box according to the co-crystallized ligand coordinates. All visualization of protein–ligand complexes were analyzed using the Autodock tools program and PyMOL molecular graphics program (https://pymol.org/2/) (DeLano, 2002). The two-dimensional (2D) schematic diagrams of protein–ligand interactions were generated by the LigPlot version (4.5.3) (https://www.ebi.ac.uk/thornton-srv/software/LIGPLOT/) (Anupama et al., 2019).

2.2.2 Preparation of lipid polymer hybrid (LPH) nanoparticles

Different LPH nanoparticles loaded with the selected drug from the docking study were prepared by a modified single-step nano-precipitation self-assembly technique (Tahir et al., 2019). Briefly, the polymer (PLGA) and the candidate drug were dissolved in acetonitrile to obtain the organic phase. LEC and tween 80 were dissolved in a 4% v/v hydroalcoholic solution, as the aqueous phase at 65 °C. Consequently, the organic phase was slowly dripped into the aqueous phase while stirring for 2 h at 65 °C. The organic to aqueous phase ratio was kept at 1:9 v/v. The resultant LPH dispersions were centrifuged at 15000 rpm for 15 min at 4 °C. The harvested pellets were washed twice with phosphate buffer saline (PBS pH 7.4), then re-suspended in the same medium for further analysis. The fluorescently labeled optimized LPH formula was prepared by dissolving the fluorescent dye (DiI) into the lipid solution at 1% w/w. Fig. 1 showed the preparation steps of LPH nanoparticles.

2.2.3 Experimental design and construction of the Box-Behnken (BBD) design

LPH formulae were optimized using BBD by Design-Expert software (Design-Expert 9.0.5.2, State-Ease Inc., USA). The statistical models and the response surfaces were explored from the constructed matrix (Bachhav et al., 2017). The selected critical process parameters (CPPs) under this study were; the PLGA amount, Drug amount, and the stirring speed were coded as A, B, C respectively. There were three levels for each variable; low (-1), medium (0), and high (+1). The critical quality attributes (CQAs) were particle size (Y_1), zeta potential (Y_2), and encapsulation efficiency (EE%) (Y_3). The quality target product profile (QTPP) of the optimized LPH formula was to achieve minimum particle size, maximum zeta potential, and maximum EE%. The determined CPPs and CQAs, as well as the required QTPP, are listed in Table 1.

The polynomial equations were statistically validated by ANOVA and all observed responses were fitted to different models (linear, two-factor interactions (2FI) and quadratic). The statistical significance of different models was assessed using various statistical indices as P-values, F values, adjusted R^2, predicted R^2 and predicted residual error sum of squares (PRESS). The 3D response surface plots were constructed by the software and the polynomial equations were authenticated. According to the highest desirability, the design space was constructed to determine the optimum CPPs required to fabricate the optimized drug-LPH with the targeted QTPP (Al-mahallawi et al., 2019).

Table 1
Levels of critical process parameters, critical quality attributes, and quality target product profile for the preparation of drug-LPH using the Box-Behnken design.

Critical process parameters (CPPs) (Coded independent variables)	Levels		
	Low (-1)	Medium (0)	High (1)
A: PLGA (mg)	5	10	15
B: Drug (mg)	10	15	20
C: Stirring speed (rpm)	500	750	1000
Critical quality attributes (CQAs) Quality target product profile (QTPP) (Responses) (Constraints)			
Y_1: Particle size (nm)	Minimize		
Y_2: Zeta potentiel (mV)	Maximize		
Y_3: EE(%)[a]	Maximize		

a EE% = Encapsulation efficiency parentage.

2.2.4 In vitro characterization of the optimized LPH formula

2.2.4.1 Particle size, size distribution, and zeta potential. The dynamic light scattering (DLS) (Zeta sizer, Malvern Instruments, UK) was used to estimate the particle size, polydispersity index (PDI), and zeta potential of the optimized LPH formula. The measurements were performed using a 90° angle at 25 °C (Abd-Elsalam et al., 2018a; Ahmed et al., 2019).

2.2.4.2 Drug encapsulation and loading efficiency (EE%, LE%). The drug EE% was measured indirectly by the ultrafiltration centrifugation method (Ishak et al., 2017). Briefly, 1 mL of the prepared LPH dispersion was added to the Amicon tube® (30,000 MWCO, Millipore, USA) and centrifuged at 15000 rpm for 15 min at 4 °C. The amount of free unentrapped drug in the filtrate was determined using a previously validated HPLC method (Dionex™, Thermo Scientific™, USA). A

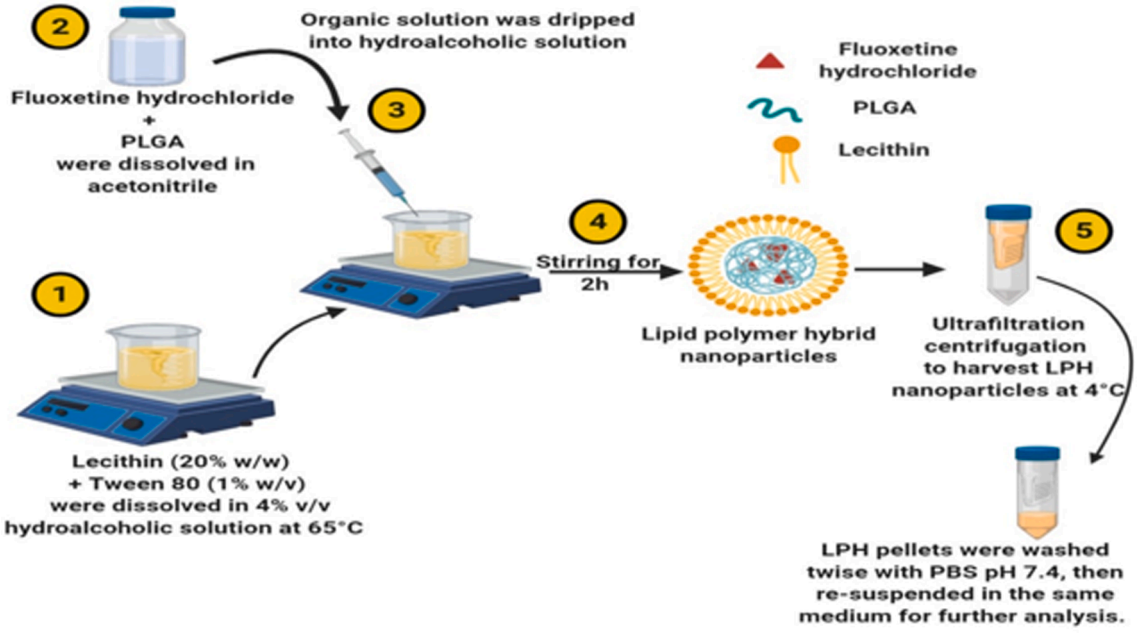

Fig. 1. Schematic representation of LPH nanoparticle preparation. The candidate drug and PLGA polymer were dissolved in acetonitrile. Lecithin and tween 80 were dissolved in 4% v/v hydroalcoholic solution and heated at 65 °C. The drug-polymer organic solution was slowly dripped into the hydroalcoholic lipid phase with magnetic stirring at 65 °C for 2 h. LPH nanoparticles were harvested by ultrafiltration centrifugation (15000 rpm, 15 min) at 4 °C and re-suspended in PBS pH 7.4 for further analysis.

reverse phase C_{18} column (150X4.6 mm, 5 μm, Hypersil ® ODS, USA) and a mobile phase consisting of acetonitrile and deionized water containing 10 mM aqueous triethylamine at a ratio of (55:45 v/v) with a flow rate of 1 mL/ min at 25 °C were employed. The UV detector was set at 226 nm. The calibration curve of the candidate drug in PBS (pH 7.4) in the concentration range of 1–100 μg/mL has a coefficient of determination (R^2) equal to 0.9994 with a limit of detection and quantification equal to 0.5 and 1 μg/mL, respectively. Moreover, the coefficient of variation percentage ranged from 2.1% to 4.9% and the accuracy for drug determination was 1.5% to 4.6% with a mean drug recovery percentage of 97.5 ± 1.16%. The EE% and LE% of the candidate drug was calculated using the following equations:

$$EE\% = \frac{\text{Thetotalamountofdrugindispersion} - \text{Amountofdrugthesupernatant}}{\text{Thetotalamountofdrugindispersion}} X100 \quad (1)$$

$$LE\% = \frac{\text{MassofdrugloadedinLPH}}{\text{Thetotalmassofdrug} - \text{LPHNPs}} \times 100 \quad (2)$$

2.2.4.3 Morphological studies. The morphological architecture of the optimized LPH was visualized by a transmission electron microscope (TEM) (Jeol, JEM-1230, Japan). Briefly, the examination was performed by depositing a drop of the dispersion on a carbon-coated copper grid (300-mesh) and dried for 10 min. Before imaging, one drop of 2% phosphotungstic acid was applied and dried for 5 min (Abd-Elsalam et al., 2018b). Moreover, the atomic force microscope (AFM) (Wet-SPM 9600, Scanning probe microscope, Shimadzu, Japan) was employed to visualize the topographical image and the 3D surface morphology of the optimized LPH dispersion. Briefly, one drop of the dispersion was deposited on a silicon wafer and air-dried. Consequently, it was scanned using a constant force model. A non-contact mode software was used in recording the AFM images under normal atmospheric conditions (Hamdi et al., 2020).

2.2.4.4 Differential scanning calorimetry. The physical state of the candidate drug within the optimized LPH was investigated by the Differential scanning calorimetry (DSC) (Shimadzu Scientific instrument, USA). The free candidate drug, drug-loaded LPH, and blank LPH nanoparticles were accurately weighed and sealed in aluminum pans. The analysis was performed under a nitrogen flow rate of 30 mL/minute to prevent oxidation. The DSC thermograms were recorded at a temperature range of 25 °C- 200 °C with a heating rate of 10 °C/ min (Elsherif et al., 2021; Tahir et al., 2019).

2.2.4.5 In vitro serum stability assay. The optimized LPH dispersion was incubated with 10 and 50% v/v fetal bovine serum (FBS) for 4 and 24 h at 37 °C. The *in vitro* serum stability was evaluated by recording the change in particle size, PDI, and zeta potential (Zhao et al., 2015).

2.2.4.6 In vitro drug release. The dialysis membrane method was employed to assess the *in vitro* drug release from the optimized LPH formula (El-Gogary et al., 2014). Briefly, A specified volume of the optimized LPH (equivalent to 2 mg of the candidate drug) was diluted with 1 mL PBS (pH 7.4). Then it was mixed with FBS (at a final concentration of 10 and 50% v/v) and added to the dialysis membrane (cut off: 10,000 Da). The dialysis bag was sealed and immersed in 25 mL of PBS (pH 7.4) at 37 ± 0.5 °C, and 100 ± 0.1 S/min. Different aliquots (0.2 mL) were withdrawn at predetermined time intervals and replaced by fresh media. The samples were analyzed using the previously validated HPLC method. The release of free drug was performed under the same conditions as a control. Moreover, the release data were fitted into different kinetics models to determine the possible release mechanism (Pardeshi et al., 2013). Additionally, the similarity factor (f_2) **(Eq. (3))** was calculated to compare the different release profiles, where the two dissolution profiles were considered similar when the f_2 value is ≥ 50 (Shah et al., 1998).

$$f_2 = 50 \times log\left[1 + \frac{1}{n}\sum (R_t - T_t)^2\right]^{-0.5} \times 100 \quad (3)$$

Where R_t is the dissolution percentage of the reference (pre-change) formula at time t, T_t is the dissolution percentage of the test (post-change) formula at time t, and n is the number of time points (Shah et al., 1998).

2.2.4.7. Short term stability study. Briefly, the optimized LPH dispersion was initially frozen at −80 °C, then primarily dried by heating the samples to −40 °C at pressure 100 μbar. The secondary drying step was performed at a temperature of 20 °C and pressure of 20 μbar." The freeze-dried optimized LPH formula was obtained after 48 h lyophilization and kept at 4 °C and 25 °C/ 60 ± 5% relative humidity (RH) (WHO, 2017) for 28 days. The change in particle size, PDI, zeta potential, and EE% was evaluated after 7, 14, 21, and 28 days as previously described (Sengel-Turk and Hascicek, 2017).

2.2.4.8. In vitro hemolytic assay. The hemolytic effect of the optimized LPH dispersion was conducted on fresh red blood cells (RBCs) of male albino rats according to the ethical committee of the faculty of the pharmacy-Cairo university with license number (PI 2077). Briefly, the blood was withdrawn on a heparinized tube from the tail vein of male albino rats (aged 2–3 months, 200 g ± 10%). The blood was then centrifugated at 4000 rpm for 10 min. The collected RBCs were subjected to different concentrations of optimized LPH formula (20–200 μg/mL) and incubated for 2 h at 37 °C. After centrifugation of samples (4000 rpm, 5 min) at 4 °C, the absorbance of the supernatant was determined at 545 nm. The negative and positive controls were prepared by incubating RBCs with PBS (pH 7.4) and 0.5% w/v Triton X-100, respectively (Hamdi et al., 2020). The percentage (%) hemolysis was calculated using the following equation:

$$\%Hemolysis = \frac{\text{absorbancesample} - \text{absorbancenegativecontrol}}{\text{absorbancepositivecontrol} - \text{absorbancenegativecontrol}} *100 \quad (4)$$

2.2.4.9. In vitro cytocompatibility assay. The *in vitro* cytocompatibility assay of the optimized LPH formula was assessed on human lung fibroblast (CCD-19Lu) Cells by MTT assay (Li et al., 2017). Briefly, cells were seeded in a 96-well plate (10,000 cells/ well) in the DMEM culture media enriched with 100 mg/mL of streptomycin, 100 units/mL of penicillin, 1% L-glutamine, and 10% heat-inactivated FBS for 24 h at 37 °C. The human lung fibroblast (CCD-19Lu) cells were then treated with serial drug concentrations ranging from 0.01 to 100 μM and incubated for 72 h. Afterward, the media was replaced with 120 μL of MTT solution for 4 h at 37 °C and 5% CO_2. The obtained formazan crystals were dissolved by a 200 μL of DMSO and then the absorbance was measured at 570 nm using a plate reader (ChroMate-4300, FL, USA). The percentage of cell viability was calculated using the following equation:

$$\%CellViability = \frac{\text{Theabsorbanceoftreatedcellsat570nm}}{\text{Theabsorbanceofuntreatedcontrolcellsat570nm}} \times 100 \quad (5)$$

2.2.4.10. In vitro cellular uptake. The flow cytometry (BD FACS Calibur™ flow cytometer, BD Biosciences) was employed to quantitatively assess the *in vitro* cellular uptake of the DiI-labelled optimized LPH. The human lung fibroblast (CCD-19Lu) cells were seeded into a 24-well plate (50,000 cells/well) for 24 h. Cells were treated with 50 nM of the DiI-labelled optimized LPH and incubated for 4 and 24 h. After incubation, the cells were washed twice with PBS (pH 7.4) and trypsinized for 5 min. The obtained cells were centrifuged (1750 rpm, 3 min) at 4 °C and re-suspended into PBS (pH 7.4). The fluorescence intensity was measured using the FL-2 detector and the collected data were

scrutinized using the FlowJo software (Oh et al., 2018).

2.2.4.11. Statistical analysis. All experiments of the present study were conducted in triplicates and the results are expressed as the mean ± SD. The difference between the two variables was compared by the Student *t*-test while the difference between groups was assessed by ANOVA followed by the Tukey HSD test. The SPSS 18 (Chicago, USA) was applied to assess the statistical analysis and the differences were considered significant at (p) value < 0.05.

3. Results and discussion

3.1. Molecular docking

Among several available crystal structures of SARS-COV-2 main protease in the PDB, The (5RGW) crystal structure was selected as the size of a co-crystalized ligand is quite similar to the size of the compounds to be docked and correct fitting in the pocket, i.e. ligand in (5RGK) is too small while ligand in (5R82) is out site the binding site (**Fig.S2).** Moreover, the docking protocol was validated by redocking the same conformer of the co-crystalized ligand with a Root Mean Square Deviation (RMSD) of 1.021 A° (**Fig.S3),** which indicated a good solution as the calculated RMSD ≤ 2.0 Å (Gohlke et al., 2000).

Docking and molecular interaction of the selected SSRIs were studied where the best 20 modes of binding with the binding site were recorded and the binding affinity values of the best mode are shown in Table.2. According to the binding energy, the affinity of different tested SSRIs to the SARS-COV-2 main protease could be arranged as follows paroxetine > reboxetine S, S > FH > reboxetine R, R > Atomoxetine > nisoxetine. Furthermore, Fig. 2 **shows** the binding interactions between different SSRIs and the SARS-COV-2 main protease. Among these compounds, only FH was able to form hydrogen bonding by the interaction of the trifluoromethyl group with the binding site residues as well as hydrophobic interactions while the other compounds only were able to bind hydrophobically. Interestingly, the presence of hydrogen bonds promotes the stability of the interaction of ligands with the active sites of protein (Chen et al., 2016; Patil et al., 2010). Moreover, Fig. 3 shows the 2D and 3D ligand–protein interaction of FH with the binding site of SARS-COV-2 main protease; FH was able to form hydrogen bonding with Histidine 163 (Fig. 3 **C, F)** and additionally sometimes can form hydrogen bonding with Serine 144 (Fig. 3 **E).**

According to the binding affinities of the studied compounds and the ligand–protein interaction, we concluded that FH could be considered as a potential SARS-COV-2 main protease inhibitor. In this study, the suggested activity of FH on COVID-19 is based on its highest binding affinity to SARS-COV-2 main protease. On the other hand, the recent observational (Hoertel et al., 2021a, 2021b) and preclinical (Carpinteiro et al., 2020) studies suggested the activity of FH on COVID-19 based on its acid sphingomyelinase inhibitory activity that decreases the ceramide concentration on the surface of the epithelial cells and consequently prevents their infection with COVID-19 (Gulbins et al., 2013).

Additionally, FH has antiviral activity against the human enteroviruses by targeting their 2C protein as previously reported (Bauer et al., 2019; Ulferts et al., 2013). Besides, its ability to reduce Coxsackievirus B4 replication (Benkahla et al., 2018). Moreover, FH inhibited the hepatitis C virus by facilitating the interferon- α-mediated antiviral effect through the activation of c-Jun amino-terminal kinases (JNK) and signal transducer and activator of transcription (STAT)-1 (Young et al., 2014). Furthermore, FH can decrease the serum level of pro-inflammatory cytokines including IL-1B, IL-6, and TNF-α (Lu et al., 2017; Ondicova et al., 2019; Sacre et al., 2010). And consequently, FH could prevent the cytokine storm of COVID-19 that is associated with respiratory failure (SARS), organ failure, and death (Xu et al., 2020; Ye et al., 2020). Therefore, FH was selected for the forthcoming formulation study to improve its therapeutic activity against COVID-19.

Table 2
The docking interaction parameters of the selected selective serotonin reuptake inhibitors with the SARS-CoV2 main protease.

Ligand	Binding free energy (kcal/mol)	Targeted amino acid	Total hydrogen bond number
Fluoxetine hydrochloride	−6.7	Histidine 163 Serine 144	2
Atomoxetine	−6	–	–
Nisoxetine	−5.7	–	–
Paroxetine	−7.3	–	–
Reboxetine R,R	−6.5	–	–
Reboxetine S.S	−6.8	–	–

3.2. Formulation and optimization of different FH loaded LPH

The candidate drug from the molecular docking study, FH, was loaded in LPH by a modified nanoprecipitation self-assembly method (Tahir et al., 2019). During this approach, the addition of the organic phase to the aqueous phase decreased the interfacial tension. Moreover, the levigation of the two phases produced turbulence which enhanced the diffusion of the water-miscible-organic solvent through the aqueous phase. Consequently, the drug and polymer migrate into the aqueous phase and form a precipitate that is considered a nucleation point for nanoparticles formation (Guterres et al., 2007).

The self-assembly of the lipids surrounding the produced polymeric core was derived by the hydrophobic interactions between their hydrophobic tail and the polymeric core, while their hydrophilic head would protrude to the external aqueous surrounding forming a homogenous surfactant stabilized LPH (Hadinoto et al., 2013). Based on the highest adjusted and predicted R^2 values with a difference below 0.2 and the least PRESS value after omitting the non-significant factors (Huang et al., 2004), the quadratic model was elected as the best fit statistical model for all responses (particle size, EE%, and zeta potential) **Tables S1-S3.**

3.2.1 Effect of different critical process parameters on particle size (Y_1)

The fabricated FH-LPH had a particle size ranging from 110.8 nm to 240.5 nm as shown in Table 3. All formulae were monodispersed systems with PDI values<0.3 (Danaei et al., 2018). **Eq. (6)** described the effect of various significant CPPs on the particle size as following:

$$Y_1 = +214.46 + 38.49A + 7.62B - 5.26C + 17.88AB + 7.9AC - 17.55A^2 - 38.88B^2 \quad (6)$$

The regression coefficients of all assessed CPPs and the ANOVA results were listed in **Table S4 and S5**, respectively. Based on Eq. (6) and **Fig. S4**, it is clear that FH-LPH particle size was positively correlated with PLGA amount **(A)**, and drug amount **(B).** The increase in polymer and drug amounts increased the viscosity of the organic phase, decreased its evaporation rate, and consequently produced a large particle size (Ravi et al., 2015). Furthermore, this viscus dispersion decreased the impact of the shear force of stirring and would prevent the breaking of the produced droplets into smaller ones (Gajra et al., 2016). Additionally, the positive coefficient of the interaction **(AB)** between PLGA amount and drug amount indicated the enhanced effect of both variables on the viscosity of the organic phase yielding LPH with a large particle size (Fig. 4**A).**

On the other hand, the FH-LPH particle size was negatively correlated with stirring speed **(C)** (**Fig. S4).** As the increase in stirring speed generates high mechanical and hydraulic shear that produces nanoparticles of small particle size (Maleki Dizaj et al., 2016). But the positive coefficient of the interaction (**AC**) between PLGA amount and the stirring speed indicated the prime effect of PLGA amount on the particle size of LPH, and the particle size was significantly increased ($P < 0.05$) (Fig. 4**B).**

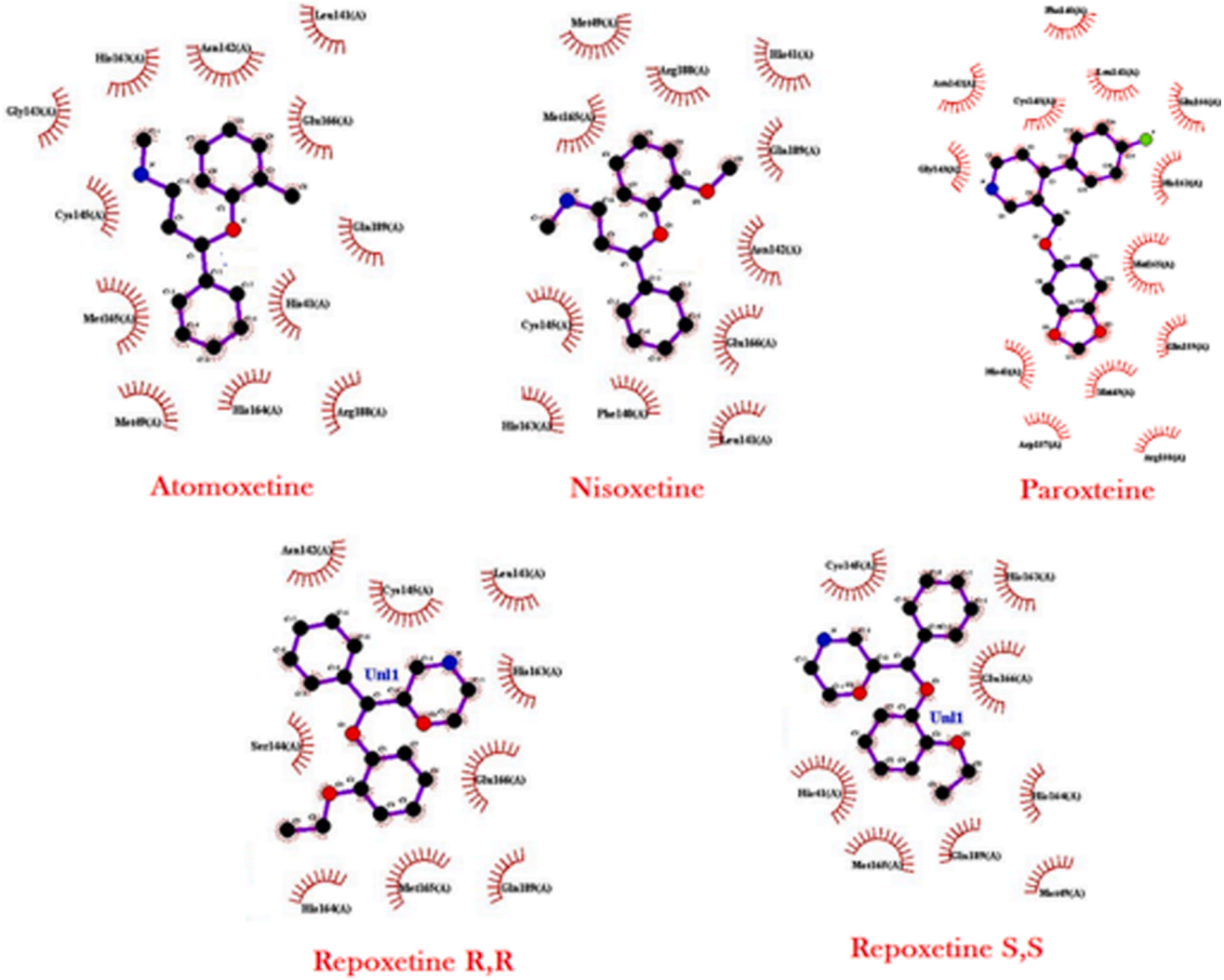

Fig. 2. LigPlot 2D schematic diagrams of protein–ligand interactions of the docked compounds. The hydrophobic contacts are represented by an arc with spokes radiating towards the ligand atoms they contact. The contacted atoms are shown with spokes radiating back.

3.2.2. Effect of different critical process parameters on FH EE% (Y_2)

The obtained FH-LPH had a drug EE% varied between 41.5% and 73.1% as shown in Table 3**.** The influence of different significant CPPs on FH EE% could be depicted in **Fig. S5** according to the following equation:

$$Y2 = +54.54 + 7.11A + 3.11B + 5.63C + 1.95AB + 5.67BC + 8.38A^2 - 3.27B^2 \quad (7)$$

Table S6 shows the regression coefficients values of each of the CPPs with a statistical significance value ($P < 0.05$) and **Table S7** shows the ANOVA results. **Eq.** (7) shows a positive correlation between all factors' effects and EE% as shown in **Fig. S5**. The PLGA amount **(A)** had the highest positive significant effect on the drug EE% ($P < 0.05$) because it formed a large core that incorporates large amounts of the drug (Gajra et al., 2015)**.** Moreover, the higher PLGA amount increased the viscosity of the organic phase and produced a large particle size, which would prevent the production of porous particles with the acquirement of a longer diffusion path for the drug that enhances the EE% (Lalani et al., 2012)**.** These results were in agreement with *Hamdi et al,* and *Tahir et al,* who reported that the increase in PLGA amount increased EE% of entecavir and doxorubicin respectively (Hamdi et al., 2020; Tahir et al., 2019)**.**

Additionally, the rise in drug amount **(B)** (a hydrophilic drug, pKa = 10, Log p = 1.2) (Kwon and Armbrust, 2008) would compensate for its leakage from the prepared nanoparticles and significantly increased its EE% ($P < 0.05$) **(Fig. S5)** (Song et al., 2008)**.** Furthermore, the rise in stirring speed **(C)** significantly increased the FH EE% (**Fig. S5**) ($P < 0.05$). During the nanoprecipitation technique, nanoparticles are formed by the interfacial phenomena, as the interfacial turbulence caused convection effects. So the solvent transport produced a physicochemical instability and formed local regions of supersaturation. Moreover, the presence of turbulence for a definite time might promote the evaporation of the organic solvent and prevents drug leakage (Salatin et al., 2017)**.**

The positive coefficient of the interaction (**AB**) between PLGA amount and drug amount indicated the significant ($P < 0.05$) synergistic effect of their interaction on the FH EE% (Fig. 5**A**)**.** As the **(AB)** interaction is associated with the formation of large particle sizes (Fig. 4**A**), which enhances the encapsulation of large amounts of the drug (Gajra et al., 2015)**.** Moreover, the positive coefficient of the interaction (**BC)** between drug amount and the stirring speed indicated the significant ($P < 0.05$) synergistic effect of their interaction on FH EE% (Fig. 5**B**)**.**

3.2.3. Effect of different critical process parameters on zeta potential (Y_3).

Table 3 shows that the fabricated FH-LPH had a zeta potential ranging from −5.5 mV to −15.3 mV. It is to be noted that the absolute values of zeta potential will be used in discussion to avoid misperception (Aziz et al., 2019)**.** The influence of different significant CPPs on zeta

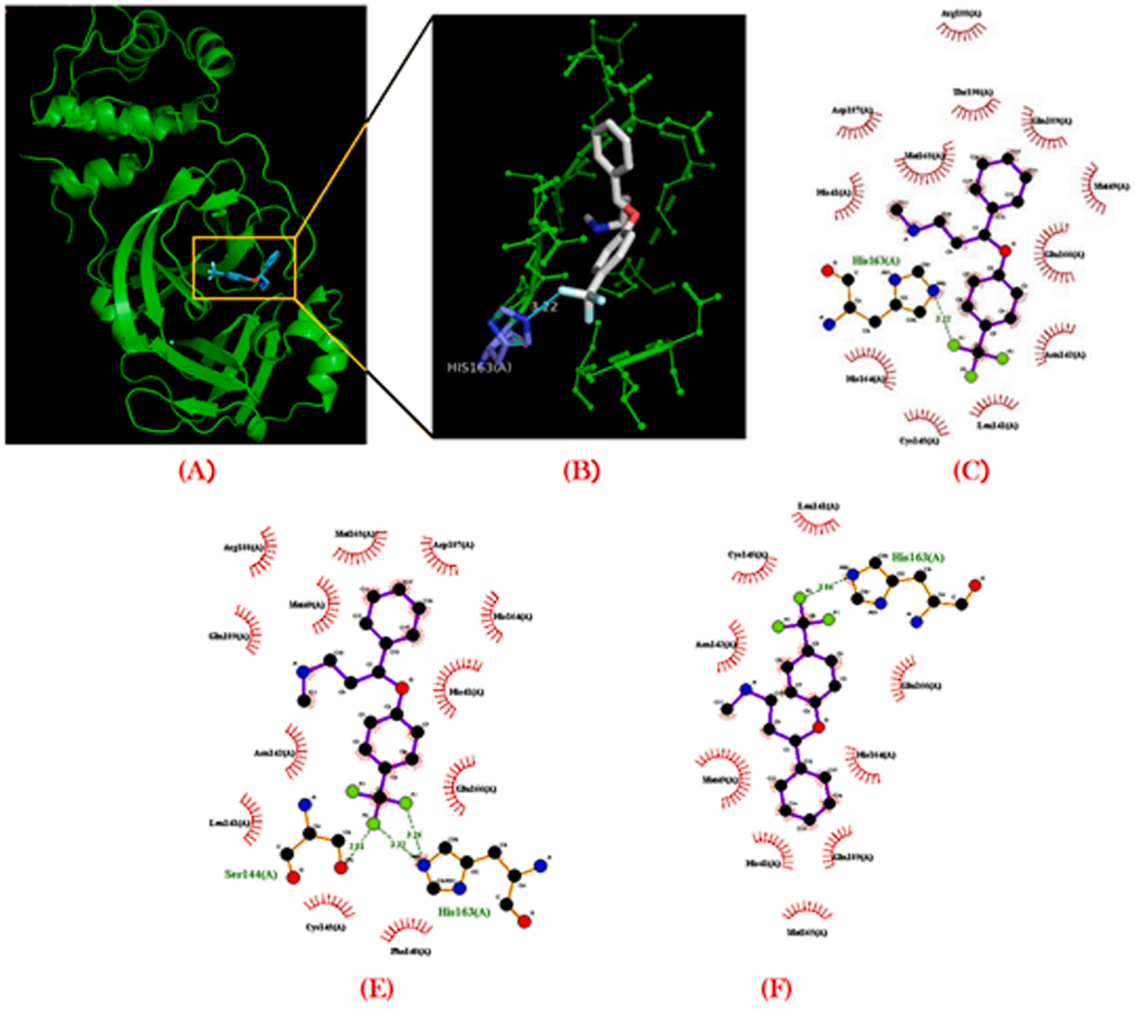

Fig. 3. (A), (B), and (C): Pymol 3D and LigPlot 2D schematic diagrams of protein–ligand interactions of the best mode of binding of Fluoxetine hydrochloride. (E) and (F): LigPlot 2D schematic diagrams of protein–ligand interactions of the subsequent best modes of binding of Fluoxetine hydrochloride. The interactions shown are those mediated by hydrogen bonds and by hydrophobic contacts. Hydrogen bonds are indicated by dashed lines between the atoms involved, while hydrophobic contacts are represented by an arc with spokes radiating towards the ligand atoms they contact. The contacted atoms are shown with spokes radiating back.

potential could be depicted from **Fig. S6** according to the following equation:

$$Y3 = +9.34 - 1.05A - 0.85B - 0.58AB - 1.72BC - 0.91A^2 + 1.39B^2 + 0.49C^2 \quad (8)$$

Table S8 shows the regression coefficient values of each of the CPPs with a statistical significance value ($P < 0.05$). Moreover, the ANOVA results demonstrated the significant effect of the CPPs ($P < 0.05$) on FH-LPH zeta potential **Table S9.**

Eq. (8) and Fig. S6 illustrated that the absolute value of zeta potential was negatively correlated with PLGA amount **(A)** and drug amount **(B).** On the contrary, it was positively correlated with the stirring speed **(C).** The cationic nature of FH might be responsible for the significant decrease in the absolute value of zeta potential ($P < 0.05$) (Pham et al., 2018**).** Furthermore, the increase in PLGA amount is associated with higher EE% of the drug (**Fig. S5)** and consequently, the absolute value of zeta potential was significantly decreased ($P < 0.05$). On the contrary, the rise in stirring speed **(C)** significantly decreased the particle size of FH-LPH ($P < 0.05$) and this might be associated with a high absolute value of zeta potential (Ding and Kan, 2017**).**

Additionally, the negative coefficient of both **(AB)** interaction between PLGA amount and drug amount and **(BC)** interaction between drug amount and stirring speed showed a significant antagonistic effect of their interactions on the absolute value of zeta potential ($P < 0.05$) (Fig. 6**A and B)**, respectively. As either **(AB)** or **(BC)** interactions associated with higher EE% of the drug (Fig. 5**).**

3.2.4. *Design space and optimization*

Design space was constructed to optimize all the investigated CPPs to fulfill QTPP criteria; minimum particle size, maximum zeta potential (absolute value), and maximum EE% (**Fig. S7-S9)**. Based on the highest desirability (combined value 0.902), one formula was selected as a checkpoint to authenticate the obtained statistical models. Table 4 **and Fig. S10-S12** illustrate its composition, where the optimum level for each factor was 5 mg, 20 mg, and 1000 rpm for PLGA amount (desirability 1), drug amount (desirability 1), and the stirring speed (desirability 1), respectively. Moreover, the comparison of the observed and predicted values of particle size (Y_1) (desirability 1), EE% (Y_2) (desirability 0.697), and zeta potential (Y_3) (desirability 1) was shown in table 4 with a % predicted error ranged between 0.3 and 3.8%. The small values of the % predicted error verified the applicability of the generated models to optimize FH-LPH (Abdelbary and Aboughaly, 2015**).** So, the optimized formula, referred to as OFH-LPH was selected for further studies.

Table 3
Experimental design matrix of the critical process parameters and the related critical quality attributes.

Run	Critical process parameters (CPPs)			Critical quality attributes (CQAs)		
	A PLGA (mg)	B Drug (mg)	C Stirring speed (rpm)	Y_1 Particle size[a,c] (nm)	Y_2 EE [b,c] (%)	Y_3 Zeta potential [a,c] (mV)
1	10	15	750	215.2±2.4	53.1±3.5	9.3±1.1
2	10	10	1000	164.8±2.2	47.2±3.7	15.3±1.4
3	15	20	750	221.4±3.5	72.7±4.1	7.2±1.2
4	10	15	750	215.2±3.7	55.2±4.2	9.3±1.6
5	5	15	1000	145.6±1.8	60.5±3.5	11.8±1.4
6	15	15	1000	240.5±2.2	73.1±2.8	10.2±1.1
7	10	15	750	213.2±3.1	55.7±3.7	9.4±1.4
8	10	15	750	213.5±3.4	53.1±4.5	9.4±1.6
9	10	15	750	215.2±2.6	55.6±3.4	9.3±1.2
10	10	20	1000	179.8±1.7	65.1±3.6	10.5±1.4
11	5	15	500	172.5±2.4	50.7±3.3	8.2±1.7
12	5	20	750	110.8±1.8	52.5±4.2	10.4±1.2
13	10	10	500	175.4±3.3	46.3±4.4	8.5±1.1
14	15	15	500	235.8±3.7	62.4±3.4	5.5±1.5
15	5	10	750	130.4±2.8	50.5±4.6	11.3±1.4
16	15	10	750	169.5±2.2	62.9±4.1	10.4±1.8
17	10	20	500	189.1±3.4	41.5±3.8	10.6±1.5

[a] Measured by DLS.
[b] Calculated as a percentage of initial drug added, determined indirectly by HPLC.
[c] Expressed as mean ± SD (n = 3).

3.3. *In vitro characterization of the selected OFH-LPH*

3.3.1. *Loading efficiency percentage (LE%)*

Table 4 revealed that the LE% of the OFH-LPH was 10.3 ± 0.4%. This result was in agreement with the LE% values of different drugs in LPH nanoparticles as amphotericin B ≈ (9%) (Asthana et al., 2015), for ropinirole hydrochloride (9.9–12.5) (Pardeshi et al., 2013), and etoposide (8–10%) (Duan et al., 2017).

3.3.2 *Morphological studies*

The TEM image of the OFH-LPH demonstrated spherical non-aggregated particles with a white polymeric core surrounded by a gray lipid shell (Fig. 7**A**) (Mandal et al., 2016). The particles have a size range of 100–120 nm which was consistent with the DLS measurements. Furthermore, the 2D and the 3D structure of the OFH-LPH nanoparticles showed scattered particles with a particle size consistent with both DLS and TEM (Fig. 7**-B, C**).

3.3.3. *Differential scanning calorimetry*

The DSC thermograms of FH, blank LPH, and OFH-LPH are illustrated in Fig. 7**D**. According to the FH thermogram, FH has a crystalline nature with a melting point at 160 °C as previously reported (Silva et al., 2007). The endothermic peak of FH was completely disappeared in the DSC thermogram of OFH-LPH indicating the transformation of the drug into the amorphous state as a result of its encapsulation in the LPH nanoparticles (Ishak et al., 2017; Mandal et al., 2016). Moreover, the PLGA polymer prevents the recrystallization of the drug during the preparation of LPH nanoparticles (Mandal et al., 2016). Additionally, both blank LPH and OFH-LPH thermograms represent an endothermic peak at 50 °C which is correlated to the glass transition temperature of PLGA (Ishak et al., 2014) which indicated a negligible effect of formulation procedures on PLGA (Sanna et al., 2015).

3.3.4. *In vitro serum stability assay*

Fig. 8**A-C** shows the effect of serum incubation on particle size, PDI, and zeta potential of OFH-LPH. The OFH-LPH was stable in 10% v/v FBS with a non-significant effect on particle size, PDI, and zeta potential at all tested time points ($P > 0.05$). Moreover, the presence of 50% v/v FBS non-significantly affects the particle size, PDI, and zeta potential of OFH-LPH ($P > 0.05$) after 4 h incubation. But after 24 h incubation, there was a significant increase in the particle size, PDI, and zeta potential of OFH-LPH ($P < 0.05$).

The negativity of the OFH-LPH surface (-10.5 mV) might be sufficient to prevent the adsorption of a low concentration of serum proteins (10% v/v FBS) by the electrostatic repulsion (Zhao et al., 2015). Contrarily, the presence of a high concentration of serum proteins (50% v/v FBS) for a long incubation time (24 h) might enhance the adsorption of a large number of serum proteins to the OFH-LPH surface and consequently, the particle size, PDI, and zeta potential were increased.

3.3.5. *In vitro FH release*

Fig. 9**A.** illustrated the *in vitro* release study in PBS (pH 7.4) with/without 10% v/v, and 50% v/v FBS. FH is a hydrophilic drug that is completely diffused through the dialysis membrane after 2 h. On the contrary, FH was released from the LPH in PBS and 10% v/v FBS in a controlled release manner and released 86.6 ± 4.5% and 92.1 ± 4.2% after 24 h, respectively with almost similar release profile ($f2$ value of 68.1%). The controlled release pattern of LPH nanoparticles might be attributed to their architecture as they consist of a polymeric core that encapsulates the drug and a lipid shell that inhibits the drug leakage (Date et al., 2018). Besides, it reduces the water penetration to the polymeric core and consequently decreases its hydrolysis rate (Hadinoto et al., 2013). On the other hand, 50% v/v FBS increased FH release and achieved 100% release after 24 h with $f2$ value of 42.5%. The high

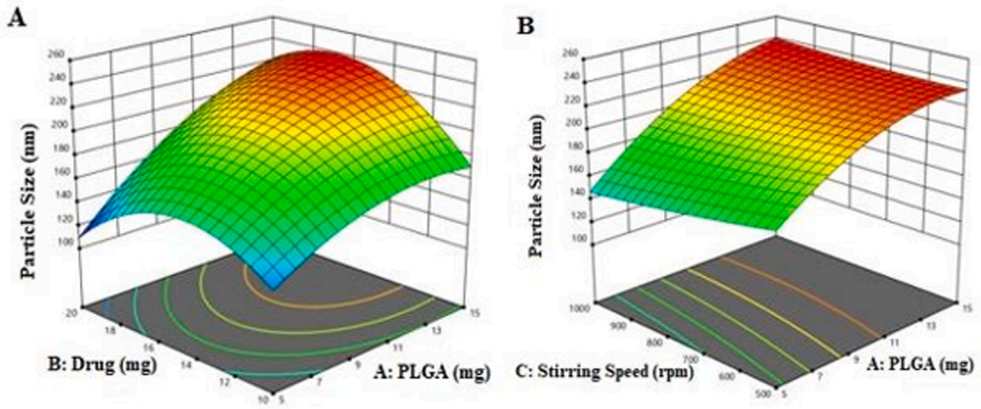

Fig. 4. Response 3D plot for the different interactions on LPH particle size (Y_1). (A) The positive interaction (AB) between PLGA and drug amounts showed a positive effect on FH-LPH particle size. (B) Interaction (AC) between PLGA amount and stirring speed showed a positive effect on FH-LPH particle size.

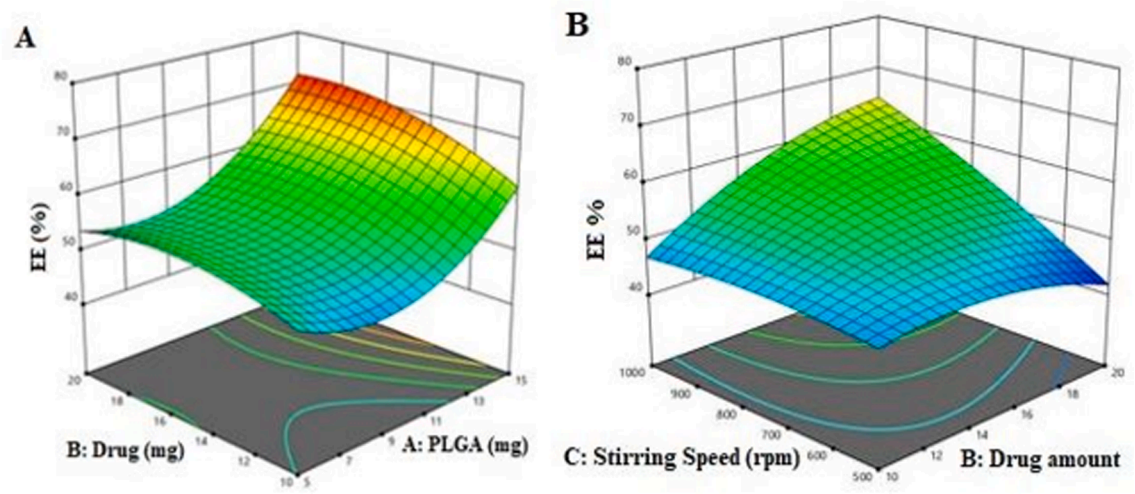

Fig. 5. Response 3D plot for the interaction of different critical process parameters on EE% (Y_2). (A) The interaction (AB) between PLGA and drug amounts had a positive influence on FH EE%. (B) The interaction (BC) between drug amount and the stirring speed had a positive influence on FH EE%.

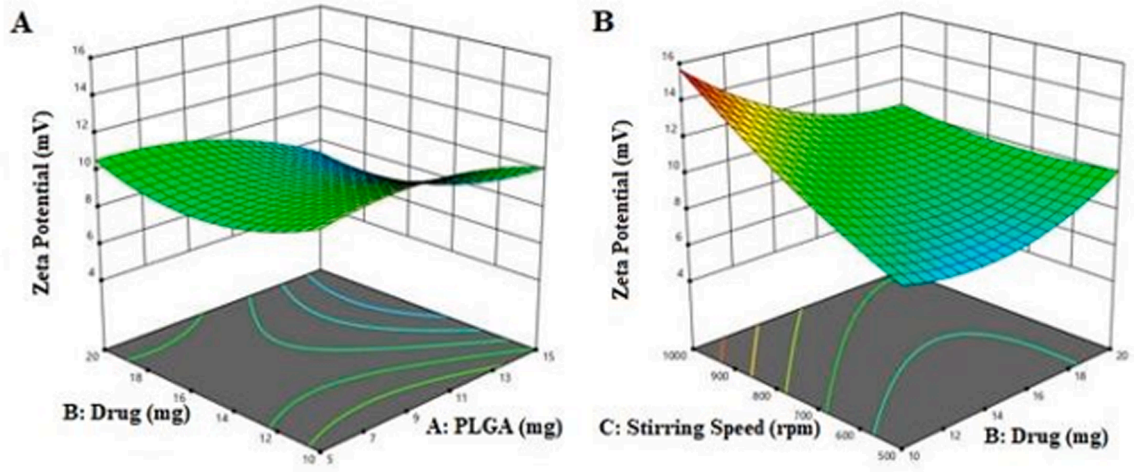

Fig. 6. Response 3D plot for the interaction of critical process parameters on zeta potential (Y_3). (A) The interaction (AB) between the PLGA and drug amounts decreased the absolute value of FH-LPH zeta potential. (B) The interaction (BC) between the drug amount and stirring speed increased the absolute value of FH-LPH zeta potential.

Table 4
The experimental and predicted particle size, EE% and zeta potential of the OFH-LPH, and the loading efficiency%.

Parameter	PLGA (mg)	FH (mg)	Stirring speed (rpm)	Experimental [c,d]	Predicted	%Predicted error	Loading efficiency%*
Particle Size [a] (nm)	5	20	1000	98.5 ± 3.5	98.2	0.3	10.3 ± 0.4%
EE [b] (%)				65.1 ± 2.7	63.5	2.5	
Zeta Potential [a] (mV)				−10.5 ± 0.45	10.9	3.8	

[a] Measured by DLS.
[b] Calculated as a percentage of initial drug added, determined indirectly by HPLC.
[c] Expressed as mean ± SD (n = 3).
[d] Statistical analysis was carried out using a student's T-test $P < 0.05$.
* Loading efficiency % was calculated for the optimized formula only.

concentration of serum proteins and lipase enzyme might induce the hydrolysis of the lipid shell and consequently enhances the polymeric core dissolution and increases the drug release (Mat Azmi et al., 2015).

The application of different kinetics models to the *in vitro* release data revealed that the diffusion mechanism was attained for the FH release profile in PBS pH7.4 with/without 10% v/v FBS with an R^2 value of 0.9969 and 0.9972, respectively. On the other hand, the FH release profile in the presence of 50% v/v FBS followed the Korsmeyer-Peppas model with an R^2 value of 0.9989 and a release exponent value of n = 0.773. Therefore, it represents a non-fickian diffusion, that resulted from the combination of both drug diffusion and polymer dissolution (Costa and Sousa Lobo, 2001; Ho et al., 2017). These results were in agreement with those of *Tahir et al.,* who reported that the doxorubicin hydrochloride release pattern from LPH obeyed the diffusion mechanism (Tahir et al., 2019).

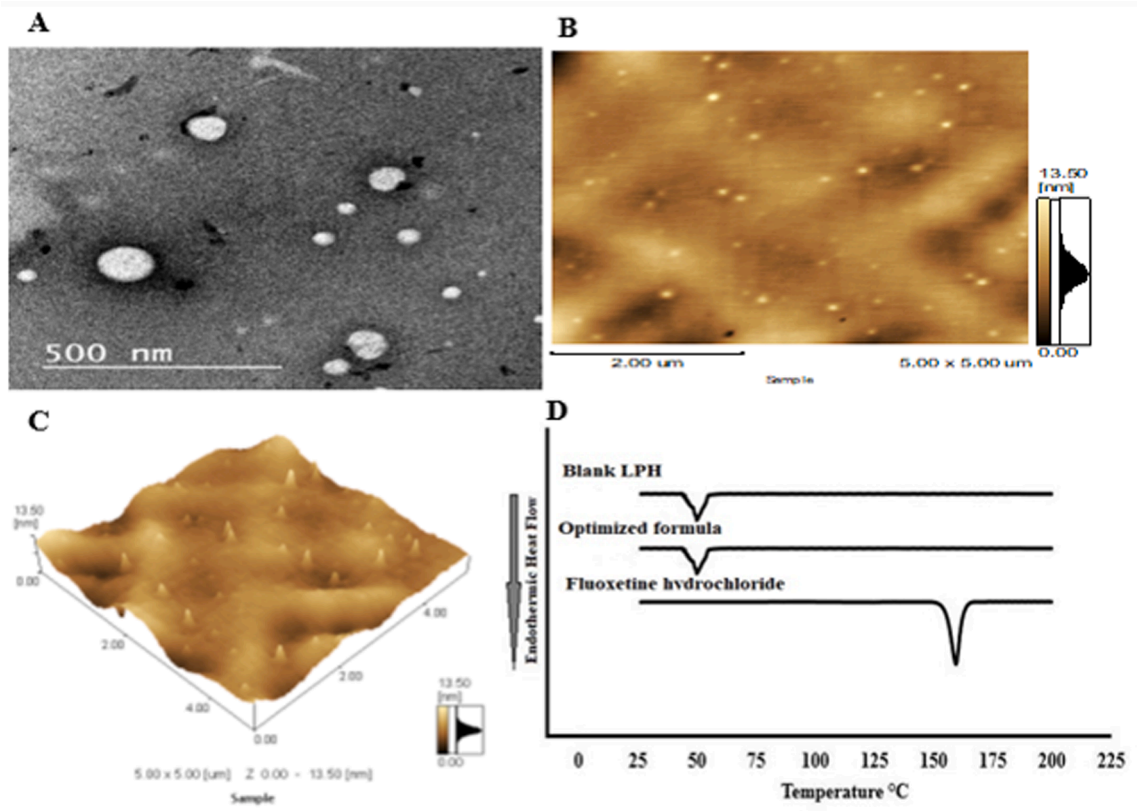

Fig. 7. *In vitro* characterization of OFH-LPH. Transmission electron micrograph of OFH-LPH (A). The 2D and 3D view of OFH-LPH by the atomic force microscope (B), (C). OFH-LPH showed a core–shell structure with a particle size in accordance with the DLS measurement. Differential scanning calorimetry thermograms of FH, blank LPH, and OFH-LPH (D). FH shows an endothermic peak at 160 °C which is completely disappeared in the thermogram of OFH-LPH. Both OFH-LPH and blank LPH show an endothermic peak at 50 °C that is correlated to the glass transition temperature of PLGA.

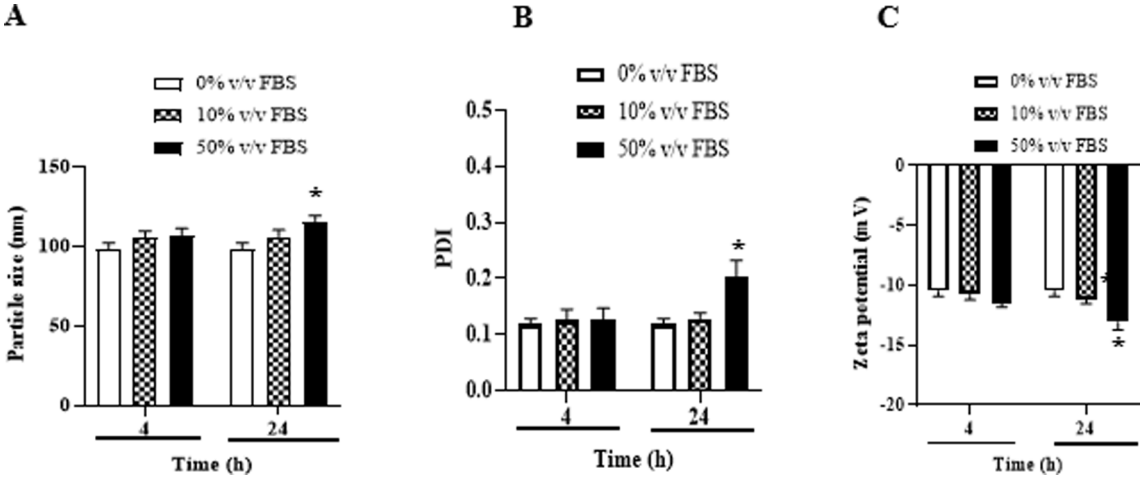

Fig. 8. The effect of serum incubation on particle size, PDI, and zeta potential of OFH-LPH. The OFH-LPH was incubated with 10 and 50% v/v FBS for 4, and 24 h then particle size (A), PDI (B), and zeta potential (C) were measured using DLS as described before. Data points represent mean and SD (n = 3). Statistical analysis was carried out using one-way ANOVA followed by the Tukey HSD test and $P < 0.05$ was considered significant. Serum proteins had a non-significant effect on OFH-LPH particle size, PDI, or zeta potential at 10% v/v FBS ($P>0.05$), but they had a significant effect on OFH-LPH particle size, PDI, or zeta potential at 50% v/v FBS after 24 h ($P < 0.05$).

3.3.6. *In vitro hemolytic assay*

A positive correlation between OFH-LPH concentration and hemolysis % (Fig. 9**B**) could be attributed to the presence of tween 80 (Ishak et al., 2017; Sun et al., 2017). However, the % hemolysis at all tested concentrations did not exceed the acceptable limit of nanocarriers (5%) according to the new consensus ASTM E2524-08-Standard test (Ishak et al., 2017). Therefore, the prepared OFH-LPH could be considered a biocompatible platform.

3.3.7. *Short term stability study*

The stability study of the OFH-LPH formula was performed on the freeze-dried form to decrease accumulation and avoid leakage of drug

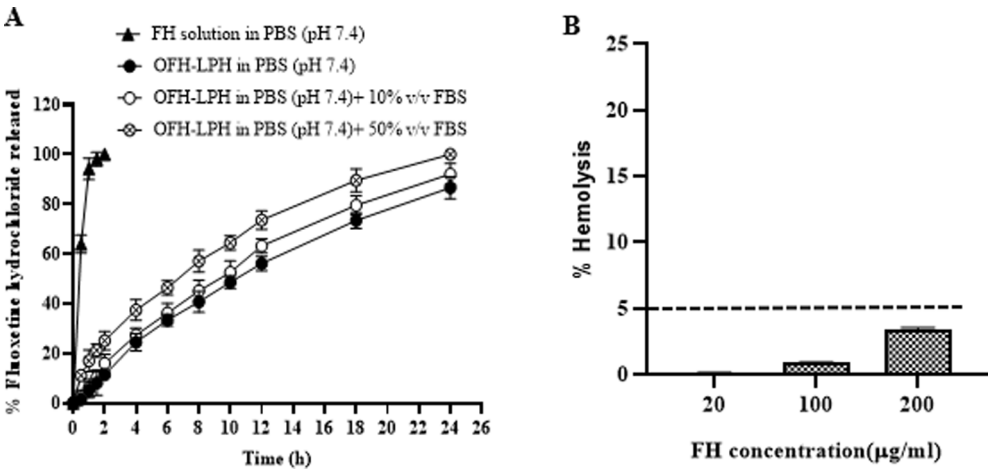

Fig. 9. *In vitro* release of FH from FH solution in PBS pH 7.4, OFH-LPH in PBS pH 7.4, OFH-LPH in PBS pH 7.4 in the presence of 10% v/v FBS, and OFH-LPH in PBS pH 7.4 in the presence of 50% v/v FBS (A). Drug concentrations in the dialysate were assessed by HPLC. Datapoint represents mean and SD (n = 3). The presence of 10% v/v FBS gave a similar release pattern to the OFH-LPH, but the presence of 50% v/v FBS increased the release rate of OFH-LPH. The *in vitro* hemolysis assay of the OFH-LPH (B). Rat RBCs were incubated with OFH-LPH at different FH concentrations (20–200 µg/mL) for 2 h at 37 °C. Positive and negative controls were 0.5% w/v Triton X-100 and PBS (pH 7.4), respectively. Samples were centrifuged at 4000 rpm for 5 min at 4 °C and the absorbance of the released hemoglobin was determined at 545 nm. Datapoint represents mean and SD (n = 3). The dotted line represents the acceptable hemolysis range. OFH-LPH is a biocompatible formula.

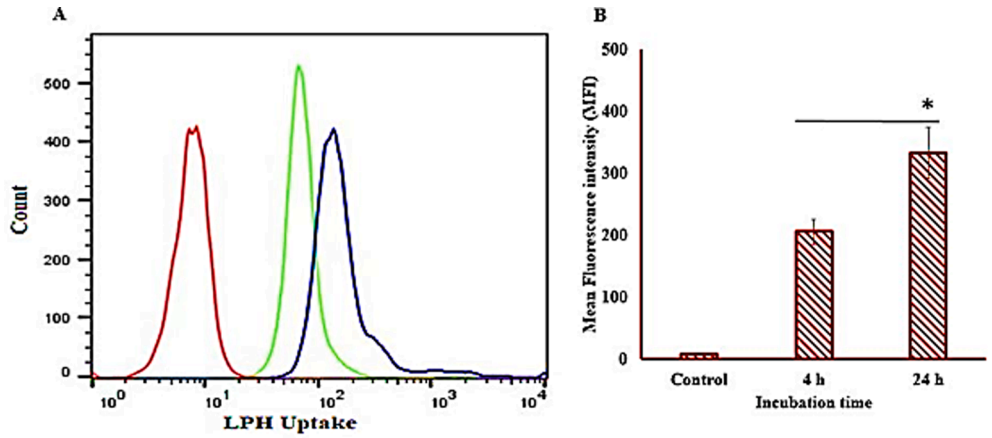

Fig. 10. Intracellular uptake of OFH-LPH in Human lung fibroblast (CCD-19Lu) Cells by flow cytometry. Cells were incubated with DiI-labelled OFH-LPH at 50 nM for 4 h (green) or 24 h (blue). Flow cytometry histogram for the uptake of DiI-labelled OFH-LPH (A). Cellular uptake was quantified by mean fluorescence intensity (MFI) using flow cytometry and FL-2 detector (B). LPH uptake was intensified in a time-dependent manner. Data points represent mean and SD (n = 3). Statistical analysis was carried out using one-way ANOVA followed by the Tukey HSD test and $P < 0.05$ was considered significant.

from the polymeric core and lipid layer during storage (Dave et al., 2017; Yuan et al., 2018). At different time intervals 7, 14, 21, and 28 days, the freeze-dried formula was redispersed in deionized water and characterized for its morphology. It has a non-significant change in its particle size, PDI, zeta potential, and EE% after 28 days of storage at 4 °C and 25 °C/ 60 ± 5% RH ($P > 0.05$) as illustrated in **Table S10**. Furthermore, these results were in agreement with the previous studies (Dave et al., 2017; Sengel-Turk and Hascicek, 2017)."

3.3.8. *In vitro cytocompatibility assay*

Fig. S13 revealed that the % cell viability of the prepared OFH-LPH formula exceeded 80% at all tested concentrations. The LPH formula loaded with FH consists of biocompatible polymer (PLGA) and lipid (LEC) therefore it improved its biocompatibility to the Human lung fibroblast (CCD-19Lu) Cells.

3.3.9. *Assessment of cellular uptake by flow cytometry*

The cellular uptake quantification of the DiI- labeled OFH-LPH (50 nM) by the Human lung fibroblast (CCD-19Lu) cells was assessed for 4 and 24 h. Where DiI is a fluorescence lipophilic carbocyanine dye that has a high fluorescence efficiency and photo-stability (Cheng et al., 2014). Additionally, it successfully labeled different lipidic and polymeric nanoparticles (Hamdi et al., 2020; Mousseau et al., 2019; Snipstad et al., 2017). The fluorescence was highly intensified following the treatment of cells with the DiI- labeled OFH-LPH in a time-dependent manner as illustrated in Fig. 10**A and B.** As the longer incubation time improved the cellular uptake by cells (Hamdi et al., 2020). Moreover, the small particle size of OFH-LPH (98.5 nm) might enhance their entry to the cells via clathrin and caveolin-mediated endocytosis (Panariti et al., 2012; Thorley et al., 2014). Therefore, LPH could efficiently improve the cellular internalization of FH into Human lung fibroblast (CCD-19Lu) Cells.

4. Conclusion

In this study, we investigate the binding affinity of different SSRIs drugs to the SARS-COV-2 main protease to assess their potential therapeutic activity against COVID-19. Among the studied drugs, FH had a promising SARS-COV-2 main protease inhibitory activity with a binding energy of (−6.7 kcal/mol) and a hydrogen bonding formation with histidine163 and serine 144 amino acids. Moreover, the encapsulation of FH in the LPH nanoparticle improved its EE%, promote its biocompatibility, and enhance its cellular uptake by the Human lung fibroblast (CCD-19Lu) cells. Therefore the fabricated FH-LPH formula represents a promising therapy for the COVID-19 pandemic. Additionally, these results along with the prior works on FH, reinforce the scientific presumption of FH efficacy in the COVID-19 pandemic, and that large-scale phase 3 trials testing FH and FH-LPH are urgently needed.

Declaration of Competing Interest

The authors declare that they have no known competing financial interests or personal relationships that could have appeared to influence the work reported in this paper.

Appendix A. Supplementary material

Supplementary data to this article can be found online at https://doi.org/10.1016/j.ijpharm.2021.121023.

References

Abd-Elsalam, W.H., El-Helaly, S.N., Ahmed, M.A., Al-mahallawi, A.M., 2018a. Preparation of novel phospholipid-based sonocomplexes for improved intestinal permeability of rosuvastatin: In vitro characterization, dynamic simulation, Caco-2 cell line permeation and in vivo assessment studies. Int. J. Pharm. 548, 375–384. https://doi.org/10.1016/j.ijpharm.2018.07.005.

Abd-Elsalam, W.H., El-Zahaby, S.A., Al-Mahallawi, A.M., 2018b. Formulation and in vivo assessment of terconazole-loaded polymeric mixed micelles enriched with Cremophor EL as dual functioning mediator for augmenting physical stability and skin delivery. Drug Deliv. 25, 484–492. https://doi.org/10.1080/10717544.2018.1436098.

Abdelbary, A.A., Aboughaly, M.H.H., 2015. Design and optimization of topical methotrexate loaded niosomes for enhanced management of psoriasis: Application of Box-Behnken design, in-vitro evaluation and in-vivo skin deposition study. Int. J. Pharm. 485, 235–243. https://doi.org/10.1016/j.ijpharm.2015.03.020.

Ahmed, M.A., Al-mahallawi, A.M., El-Helaly, S.N., Abd-Elsalam, W.H., 2019. The effect of the saturation degree of phospholipid on the formation of a novel self-assembled nano-micellar complex carrier with enhanced intestinal permeability. Int. J. Pharm. 569, 118567 https://doi.org/10.1016/j.ijpharm.2019.118567.

Al-mahallawi, A.M., Fares, A.R., Abd-Elsalam, W.H., 2019. Enhanced Permeation of Methotrexate via Loading into Ultra-permeable Niosomal Vesicles: Fabrication, Statistical Optimization, Ex Vivo Studies, and In Vivo Skin Deposition and Tolerability. AAPS PharmSciTech 20. https://doi.org/10.1208/s12249-019-1380-5.

Allouche, A., 2012. Software News and Updates Gabedit — A Graphical User Interface for Computational Chemistry Softwares. J. Comput. Chem. 32, 174–182. https://doi.org/10.1002/jcc.

Anupama, R., Lulu, S., Madhusmita, R., Vino, S., Mukherjee, A., Babu, S., 2019. Insights into the interaction of key biofilm proteins in Pseudomonas aeruginosa PAO1 with TiO2 nanoparticle: An in silico analysis. J. Theor. Biol. 462, 12–25. https://doi.org/10.1016/j.jtbi.2018.10.057.

Asthana, S., Jaiswal, A.K., Gupta, P.K., Dube, A., Chourasia, M.K., 2015. Th-1 biased immunomodulation and synergistic antileishmanial activity of stable cationic lipid-polymer hybrid nanoparticle: Biodistribution and toxicity assessment of encapsulated amphotericin B. Eur. J. Pharm. Biopharm. 89, 62–73. https://doi.org/10.1016/j.ejpb.2014.11.019.

Aziz, D.E., Abdelbary, A.A., Elassasy, A.I., 2019. Investigating superiority of novel bilosomes over niosomes in the transdermal delivery of diacerein: in vitro characterization, ex vivo permeation and in vivo skin deposition study. J. Liposome Res. 29, 73–85. https://doi.org/10.1080/08982104.2018.1430831.

Bachhav, S.S., Dighe, V.D., Kotak, D., Devarajan, P.V., 2017. Rifampicin Lipid-Polymer hybrid nanoparticles (LIPOMER) for enhanced Peyer's patch uptake. Int. J. Pharm. 532, 612–622. https://doi.org/10.1016/j.ijpharm.2017.09.040.

Bauer, L., Manganaro, R., Zonsics, B., Strating, J.R.P.M., El Kazzi, P., Lorenzo Lopez, M., Ulferts, R., Van Hoey, C., Maté, M.J., Langer, T., Coutard, B., Brancale, A., Van Kuppeveld, F.J.M., 2019. Fluoxetine Inhibits Enterovirus Replication by Targeting the Viral 2C Protein in a Stereospecific Manner. ACS Infect. Dis. 5, 1609–1623. https://doi.org/10.1021/acsinfecdis.9b00179.

Benkahla, M.A., Alidjinou, E.K., Sane, F., Desailloud, R., Hober, D., 2018. Fluoxetine can inhibit coxsackievirus-B4 E2 in vitro and in vivo. Antiviral Res. 159, 130–133. https://doi.org/10.1016/j.antiviral.2018.10.002.

Carlesso, A., Chintha, C., Gorman, A.M., Samali, A., Eriksson, L.A., 2019. Merits and pitfalls of conventional and covalent docking in identifying new hydroxyl aryl aldehyde like compounds as human IRE1 inhibitors. Sci. Rep. 9, 1–10. https://doi.org/10.1038/s41598-019-39939-z.

Carpinteiro, A., Edwards, M.J., Hoffmann, M., Kochs, G., Gripp, B., Weigang, S., Adams, C., Carpinteiro, E., Gulbins, A., Keitsch, S., Sehl, C., Soddemann, M., Wilker, B., Kamler, M., Bertsch, T., Lang, K.S., Patel, S., Wilson, G.C., Walter, S., Hengel, H., Pöhlmann, S., Lang, P.A., Kornhuber, J., Becker, K.A., Ahmad, S.A., Fassbender, K., Gulbins, E., 2020. Pharmacological Inhibition of Acid Sphingomyelinase Prevents Uptake of SARS-CoV-2 by Epithelial Cells. Cell Reports Med. 1, 100142 https://doi.org/10.1016/j.xcrm.2020.100142.

Carpinteiro, A., Gripp, B., Hoffmann, M., Pöhlmann, S., Hoertel, N., Edwards, M.J., Kamler, M., Kornhuber, J., Becker, K.A., Gulbins, E., 2021. Inhibition of acid sphingomyelinase by ambroxol prevents SARS-CoV-2 entry into epithelial cells. J. Biol. Chem. 296 https://doi.org/10.1016/j.jbc.2021.100701.

Chen, D., Oezguen, N., Urvil, P., Ferguson, C., Dann, S.M., Savidge, T.C., 2016. Regulation of protein-ligand binding affinity by hydrogen bond pairing. Sci. Adv. 2, e1501240 https://doi.org/10.1126/sciadv.1501240.

Cheng, C., Trzcinski, O., Doering, L.C., 2014. Fluorescent labeling of dendritic spines in cell cultures with the carbocyanine dye "Dil". Front. Neuroanat. 8, 1–8. https://doi.org/10.3389/fnana.2014.00030.

Costa, P., Sousa Lobo, J.M., 2001. Modeling and comparison of dissolution profiles. Eur. J. Pharm. Sci. 13, 123–133. https://doi.org/10.1016/S0928-0987(01)00095-1.

Danaei, M., Dehghankhold, M., Ataei, S., Hasanzadeh Davarani, F., Javanmard, R., Dokhani, A., Khorasani, S., Mozafari, M.R., 2018. Impact of particle size and polydispersity index on the clinical applications of lipidic nanocarrier systems. Pharmaceutics 10, 1–17. https://doi.org/10.3390/pharmaceutics10020057.

Date, T., Nimbalkar, V., Kamat, J., Mittal, A., Mahato, R.I., Chitkara, D., 2018. Lipid-polymer hybrid nanocarriers for delivering cancer therapeutics. J. Control. Release 271, 60–73. https://doi.org/10.1016/j.jconrel.2017.12.016.

Dave, V., Yadav, R.B., Kushwaha, K., Yadav, S., Sharma, S., Agrawal, U., 2017. Lipid-polymer hybrid nanoparticles: Development & statistical optimization of norfloxacin for topical drug delivery system. Bioact. Mater. 2, 269–280. https://doi.org/10.1016/j.bioactmat.2017.07.002.

Dechaumes, A., Nekoua, M.P., Belouzard, S., Sane, F., Engelmann, I., Dubuisson, J., Alidjinou, E.K., Hober, D., 2021. Fluoxetine Can Inhibit SARS-CoV-2 In Vitro. Microorganisms 9, 339. https://doi.org/10.3390/microorganisms9020339.

Diez-Quevedo, C., Iglesias-González, M., Giralt-López, M., Rangil, T., Sanagustin, D., Moreira, M., López-Ramentol, M., Ibáñez-Caparrós, A., Lorán, M.-E., Bustos-Cardona, T., Menéndez-Cuiñas, I., Mundo-Cid, P., Blanco-Presas, L., de Pablo, J., Cuevas-Esteban, J., 2021. Mental disorders, psychopharmacological treatments, and mortality in 2150 COVID-19 Spanish inpatients. Acta Psychiatr. Scand. 143, 526–534. https://doi.org/10.1111/acps.13304.

Ding, Y., Kan, J., 2017. Optimization and characterization of high pressure homogenization produced chemically modified starch nanoparticles. J. Food Sci. Technol. 54, 4501–4509. https://doi.org/10.1007/s13197-017-2934-8.

Duan, R., Li, C., Wang, F., Yangi, J.C., 2017. Polymer–lipid hybrid nanoparticles-based paclitaxel and etoposide combinations for the synergistic anticancer efficacy in osteosarcoma. Colloids Surfaces B Biointerfaces 159, 880–887. https://doi.org/10.1016/j.colsurfb.2017.08.042.

El-Gogary, R.I., Rubio, N., Wang, J.T.W., Al-Jamal, W.T., Bourgognon, M., Kafa, H., Naeem, M., Klippstein, R., Abbate, V., Leroux, F., Bals, S., Van Tendeloo, G., Kamel, A.O., Awad, G.A.S., Mortada, N.D., Al-Jamal, K.T., 2014. Polyethylene glycol conjugated polymeric nanocapsules for targeted delivery of quercetin to folate-expressing cancer cells in vitro and in vivo. ACS Nano 8, 1384–1401. https://doi.org/10.1021/nn405155b.

Elmezayen, A.D., Al-Obaidi, A., Şahin, A.T., Yelekçi, K., 2020. Drug repurposing for coronavirus (COVID-19): in silico screening of known drugs against coronavirus 3CL hydrolase and protease enzymes. J. Biomol. Struct. Dyn. 1–13 https://doi.org/10.1080/07391102.2020.1758791.

Elsherif, N.I., Al-Mahallawi, A.M., Abdelkhalek, A.A., Shamma, R.N., 2021. Investigation of the Potential of Nebivolol Hydrochloride-Loaded Chitosomal Systems for Tissue Regeneration. In Vitro Characterization and In Vivo Assessment. Pharmaceutics 13, 1–22. https://doi.org/10.3390/pharmaceutics13050700.

Gajra, B., Dalwadi, C., Patel, R., 2015. Formulation and optimization of itraconazole polymeric lipid hybrid nanoparticles (Lipomer) using box behnken design. DARU. J. Pharm. Sci. 23, 1–15. https://doi.org/10.1186/s40199-014-0087-0.

Gajra, B., Patel, R.R., Dalwadi, C., 2016. Formulation, optimization and characterization of cationic polymeric nanoparticles of mast cell stabilizing agent using the Box-Behnken experimental design. Drug Dev. Ind. Pharm. 42, 747–757. https://doi.org/10.3109/03639045.2015.1093496.

Gil, C., Ginex, T., Maestro, I., Nozal, V., Barrado-Gil, L., Cuesta-Geijo, M.Á., Urquiza, J., Ramírez, D., Alonso, C., Campillo, N.E., Martinez, A., 2020. COVID-19: Drug Targets and Potential Treatments. J. Med. Chem. 63, 12359–12386. https://doi.org/10.1021/acs.jmedchem.0c00606.

Gohlke, H., Hendlich, M., Klebe, G., 2000. Knowledge-based scoring function to predict protein-ligand interactions. J. Mol. Biol. 295, 337–356. https://doi.org/10.1006/jmbi.1999.3371.

Gordon, D.E., Jang, G.M., Bouhaddou, M., Xu, J., Obernier, K., White, K.M., O'Meara, M. J., Rezelj, V.V., Guo, J.Z., Swaney, D.L., Tummino, T.A., Hüttenhain, R., Kaake, R. M., Richards, A.L., Tutuncuoglu, B., Foussard, H., Batra, J., Haas, K., Modak, M., Kim, M., Haas, P., Polacco, B.J., Braberg, H., Fabius, J.M., Eckhardt, M., Soucheray, M., Bennett, M.J., Cakir, M., McGregor, M.J., Li, Q., Meyer, B., Roesch, F., Vallet, T., Mac Kain, A., Miorin, L., Moreno, E., Naing, Z.Z.C., Zhou, Y., Peng, S., Shi, Y., Zhang, Z., Shen, W., Kirby, I.T., Melnyk, J.E., Chorba, J.S., Lou, K., Dai, S.A., Barrio-Hernandez, I., Memon, D., Hernandez-Armenta, C., Lyu, J., Mathy, C.J.P., Perica, T., Pilla, K.B., Ganesan, S.J., Saltzberg, D.J., Rakesh, R., Liu, X., Rosenthal, S.B., Calviello, L., Venkataramanan, S., Liboy-Lugo, J., Lin, Y., Huang, X.-P., Liu, Y., Wankowicz, S.A., Bohn, M., Safari, M., Ugur, F.S., Koh, C., Savar, N.S., Tran, Q.D., Shengjuler, D., Fletcher, S.J., O'Neal, M.C., Cai, Y., Chang, J. C.J., Broadhurst, D.J., Klippsten, S., Sharp, P.P., Wenzell, N.A., Kuzuoglu-Ozturk, D., Wang, H.-Y., Trenker, R., Young, J.M., Cavero, D.A., Hiatt, J., Roth, T.L., Rathore, U., Subramanian, A., Noack, J., Hubert, M., Stroud, R.M., Frankel, A.D., Rosenberg, O. S., Verba, K.A., Agard, D.A., Ott, M., Emerman, M., Jura, N., von Zastrow, M., Verdin, E., Ashworth, A., Schwartz, O., d'Enfert, C., Mukherjee, S., Jacobson, M., Malik, H.S., Fujimori, D.G., Ideker, T., Craik, C.S., Floor, S.N., Fraser, J.S., Gross, J. D., Sali, A., Roth, B.L., Ruggero, D., Taunton, J., Kortemme, T., Beltrao, P., Vignuzzi, M., García-Sastre, A., Shokat, K.M., Shoichet, B.K., Krogan, N.J., 2020. A SARS-CoV-2 protein interaction map reveals targets for drug repurposing. Nature 583, 459–468. https://doi.org/10.1038/s41586-020-2286-9.

Gulbins, E., Palmada, M., Reichel, M., Lüth, A., Böhmer, C., Amato, D., Müller, C.P., Tischbirek, C.H., Groemer, T.W., Tabatabai, G., Becker, K.A., Tripal, P., Staedtler, S., Ackermann, T.F., van Brederode, J., Alzheimer, C., Weller, M., Lang, U.E., Kleuser, B., Grassmé, H., Kornhuber, J., 2013. Acid sphingomyelinase–ceramide

system mediates effects of antidepressant drugs. Nat. Med. 19, 934–938. https://doi.org/10.1038/nm.3214.
Guterres, S.S., Alves, M.P., Pohlmann, A.R., 2007. Polymeric Nanoparticles, Nanospheres and Nanocapsules, for Cutaneous Applications. Drug Target Insights 2, 147–157. https://doi.org/10.1177/117739280700200002.
Hadinoto, K., Sundaresan, A., Cheow, W.S., 2013. Lipid-polymer hybrid nanoparticles as a new generation therapeutic delivery platform: A review. Eur. J. Pharm. Biopharm. 85, 427–443. https://doi.org/10.1016/j.ejpb.2013.07.002.
Halperin, D., Reber, G., 2007. Influence of antidepressants on hemostasis. Dialogues Clin. Neurosci. 9, 47–59. 10.31887/DCNS.2007.9.1/dhalperin.
Hamdi, M., Abdel-Bar, H.M., Elmowafy, E., Al-Jamal, K.T., Awad, G.A.S., 2020. An integrated vitamin E-coated polymer hybrid nanoplatform: A lucrative option for an enhanced in vitro macrophage retention for an anti-hepatitis B therapeutic prospect. PLoS One 15, 1–25. https://doi.org/10.1371/journal.pone.0227231.
Hamed, M.G.M., Hagag, R.S., 2020. The possible immunoregulatory and anti-inflammatory effects of selective serotonin reuptake inhibitors in coronavirus disease patients. Med. Hypotheses 144, 110140. https://doi.org/10.1016/j.mehy.2020.110140.
Ho, H.N., Laidmäe, I., Kogermann, K., Lust, A., Meos, A., Nguyen, C.N., Heinämäki, J., 2017. Development of electrosprayed artesunate-loaded core–shell nanoparticles. Drug Dev. Ind. Pharm. 43, 1134–1142. https://doi.org/10.1080/03639045.2017.1300163.
Hoertel, N., Sánchez-Rico, M., Gulbins, E., Kornhuber, J., Carpinteiro, A., Abellán, M., de la Muela, P., Vernet, R., Beeker, N., Neuraz, A., Delcuze, A., Alvarado, J.M., Meneton, P., Limosin, F., 2021a. Association between Psychotropic Medications Functionally Inhibiting Acid Sphingomyelinase and reduced risk of Intubation or Death among Individuals with Mental Disorder and Severe COVID-19: an Observational Study. medRxiv 2021.02.18.21251997. 10.1101/2021.02.18.21251997.
Hoertel, N., Sánchez-Rico, M., Gulbins, E., Kornhuber, J., Carpinteiro, A., Lenze, E.J., Reiersen, A.M., Abellán, M., de la Muela, P., Vernet, R., Blanco, C., Cougoule, C., Beeker, N., Neuraz, A., Gorwood, P., Alvarado, J.M., Meneton, P., Limosin, F., AP-HP / Université de Paris / INSERM COVID-19 research collaboration "Entrepôt de Données de Santé" AP-HP Consortium, A.-H.C.C.D.R.I., 2021b. Association Between FIASMAs and Reduced Risk of Intubation or Death in Individuals Hospitalized for Severe COVID-19: An Observational Multicenter Study. Clin. Pharmacol. Ther. n/a. 10.1002/cpt.2317.
Hoertel, N., Sánchez-Rico, M., Vernet, R., Beeker, N., Jannot, A.-S., Neuraz, A., Salamanca, E., Paris, N., Daniel, C., Gramfort, A., Lemaitre, G., Bernaux, M., Bellamine, A., Lemogne, C., Airagnes, G., Burgun, A., Limosin, F., Initiative, O. behalf of A.-H./ U./ I.C.-19 R.C. and A.-H.C.C.D.R., 2021c. Association between antidepressant use and reduced risk of intubation or death in hospitalized patients with COVID-19: results from an observational study. Mol. Psychiatry. 10.1038/s41380-021-01021-4.
Hoertel, N., Sánchez Rico, M., Vernet, R., Beeker, N., Jannot, A.-S., Neuraz, A., Salamanca, E., Paris, N., Daniel, C., Gramfort, A., Lemaitre, G., Bernaux, M., Bellamine, A., Lemogne, C., Airagnes, G., Burgun, A., Limosin, F., 2020. SSRIs and SNRIs and Risk of Death or Intubation in COVID-19: Results from an Observational Study. medRxiv 2020.07.09.20143339. 10.1101/2020.07.09.20143339.
Hoffmann, M., Kleine-Weber, H., Schroeder, S., Krüger, N., Herrler, T., Erichsen, S., Schiergens, T.S., Herrler, G., Wu, N.H., Nitsche, A., Müller, M.A., Drosten, C., Pöhlmann, S., 2020. SARS-CoV-2 Cell Entry Depends on ACE2 and TMPRSS2 and Is Blocked by a Clinically Proven Protease Inhibitor. Cell 181, 271–280.e8. https://doi.org/10.1016/j.cell.2020.02.052.
Hojyo, S., Uchida, M., Tanaka, K., Hasebe, R., Tanaka, Y., Murakami, M., Hirano, T., 2020. How COVID-19 induces cytokine storm with high mortality. Inflamm. Regen. 40, 37. https://doi.org/10.1186/s41232-020-00146-3.
Huang, Y. Bin, Tsai, Y.H., Yang, W.C., Chang, J.S., Wu, P.C., Takayama, K., 2004. Once-daily propranolol extended-release tablet dosage form: Formulation design and in vitro/in vivo investigation. Eur. J. Pharm. Biopharm. 58, 607–614. https://doi.org/10.1016/j.ejpb.2004.03.037.
Huang, H., Zhang, G., Zhou, Y., Lin, C., Chen, S., Lin, Y., Mai, S., Huang, Z., 2018. Reverse screening methods to search for the protein targets of chemopreventive compounds. Front. Chem. 6, 1–28. https://doi.org/10.3389/fchem.2018.00138.
Ishak, R.A.H., Mortada, N.D., Zaki, N.M., El-Shamy, A.E.H.A., Awad, G.A.S., 2014. Impact of microparticle formulation approaches on drug burst release: A level A IVIVC. J. Microencapsul. 31, 674–684. https://doi.org/10.3109/02652048.2014.913724.
Ishak, R.A.H., Mostafa, N.M., Kamel, A.O., 2017. Stealth lipid polymer hybrid nanoparticles loaded with rutin for effective brain delivery – comparative study with the gold standard (Tween 80): Optimization, characterization and biodistribution. Drug Deliv. 24, 1874–1890. https://doi.org/10.1080/10717544.2017.1410263.
Jiang, L., Lee, H.W., Loo, S.C.J., 2020. Therapeutic lipid-coated hybrid nanoparticles against bacterial infections. RSC Adv. 10, 8497–8517. https://doi.org/10.1039/c9ra10921h.
Kennedy, S.H., Lam, R.W., McIntyre, R.S., Tourjman, S.V., Bhat, V., Blier, P., Hasnain, M., Jollant, F., Levitt, A.J., MacQueen, G.M., McInerney, S.J., McIntosh, D., Milev, R.V., Müller, D.J., Parikh, S.V., Pearson, N.L., Ravindran, A.V., Uher, R., 2016. Canadian Network for Mood and Anxiety Treatments (CANMAT) 2016 clinical guidelines for the management of adults with major depressive disorder: Section 3. Pharmacological Treatments. Can. J. Psychiatry 61, 540–560. https://doi.org/10.1177/0706743716659417.
Köhler, C.A., Freitas, T.H., Stubbs, B., Maes, M., Solmi, M., Veronese, N., de Andrade, N. Q., Morris, G., Fernandes, B.S., Brunoni, A.R., Herrmann, N., Raison, C.L., Miller, B. J., Lanctôt, K.L., Carvalho, A.F., 2018. Peripheral Alterations in Cytokine and Chemokine Levels After Antidepressant Drug Treatment for Major Depressive Disorder: Systematic Review and Meta-Analysis. Mol. Neurobiol. 55, 4195–4206. https://doi.org/10.1007/s12035-017-0632-1.
Kölzer, M., Werth, N., Sandhoff, K., 2004. Interactions of acid sphingomyelinase and lipid bilayers in the presence of the tricyclic antidepressant desipramine. FEBS Lett. 559, 96–98. https://doi.org/10.1016/S0014-5793(04)00033-X.
Kumar, S., Zhi, K., Mukherji, A., Gerth, K., 2020. Repurposing antiviral protease inhibitors using extracellular vesicles for potential therapy of COVID-19. Viruses 12, 1–15. https://doi.org/10.3390/v12050486.
Kwon, J.W., Armbrust, K.L., 2008. Aqueous solubility, n-octanol-water partition coefficient, and sorption of five selective serotonin reuptake inhibitors to sediments and soils. Bull. Environ. Contam. Toxicol. 81, 128–135. https://doi.org/10.1007/s00128-008-9401-1.
L DeLano, W., 2002. Pymol: An open-source molecular graphics tool. {CCP4} Newsl. Protein Crystallogr. 40, 1–8.
Lalani, J., Raichandani, Y., Mathur, R., Lalan, M., Chutani, K., Mishra, A.K., Misra, A., 2012. Comparative receptor based brain delivery of tramadol-loaded poly(lactic-co-glycolic acid) nanoparticles. J. Biomed. Nanotechnol. 8, 918–927. https://doi.org/10.1166/jbn.2012.1462.
Lenze, E.J., Mattar, C., Zorumski, C.F., Stevens, A., Schweiger, J., Nicol, G.E., Miller, J.P., Yang, L., Yingling, M., Avidan, M.S., Reiersen, A.M., 2020. Fluvoxamine vs Placebo and Clinical Deterioration in Outpatients With Symptomatic COVID-19: A Randomized Clinical Trial. JAMA 324, 2292–2300. https://doi.org/10.1001/jama.2020.22760.
Li, F., Mei, H., Gao, Y., Xie, X., Nie, H., Li, T., Zhang, H., Jia, L., 2017. Co-delivery of oxygen and erlotinib by aptamer-modified liposomal complexes to reverse hypoxia-induced drug resistance in lung cancer. Biomaterials 145, 56–71. https://doi.org/10.1016/j.biomaterials.2017.08.030.
Liu, C., Zhou, Q., Li, Y., Garner, L.V., Watkins, S.P., Carter, L.J., Smoot, J., Gregg, A.C., Daniels, A.D., Jervey, S., Albaiu, D., 2020. Research and Development on Therapeutic Agents and Vaccines for COVID-19 and Related Human Coronavirus Diseases. ACS Cent. Sci. 6, 315–331. https://doi.org/10.1021/acscentsci.0c00272.
Lu, Y., Ho, C.S., Liu, X., Chua, A.N., Wang, W., McIntyre, R.S., Ho, R.C., 2017. Chronic administration of fluoxetine and pro-inflammatory cytokine change in a rat model of depression. PLoS One 12, 1–14. https://doi.org/10.1371/journal.pone.0186700.
Maleki Dizaj, S., Lotfipour, F., Barzegar-Jalali, M., Zarrintan, M.H., Adibkia, K., 2016. Application of Box-Behnken design to prepare gentamicin-loaded calcium carbonate nanoparticles. Artif. Cells, Nanomedicine Biotechnol. 44, 1475–1481. https://doi.org/10.3109/21691401.2015.1042108.
Mandal, B., Mittal, N.K., Balabathula, P., Thoma, L.A., Wood, G.C., 2016. Development and in vitro evaluation of core-shell type lipid-polymer hybrid nanoparticles for the delivery of erlotinib in non-small cell lung cancer. Eur. J. Pharm. Sci. 81, 162–171. https://doi.org/10.1016/j.ejps.2015.10.021.
Marín-Corral, J., Rodríguez-Morató, J., Gomez-Gomez, A., Pascual-Guardia, S., Muñoz-Bermúdez, R., Salazar-Degracia, A., Pérez-Terán, P., Restrepo, M.I., Khymenets, O., Haro, N., Masclans, J.R., Pozo, O.J., 2021. Metabolic Signatures Associated with Severity in Hospitalized COVID-19 Patients. Int. J. Mol. Sci. 22, 1–14. https://doi.org/10.3390/ijms22094794.
Mat Azmi, I.D., Wu, L., Wibroe, P.P., Nilsson, C., Østergaard, J., Stürup, S., Gammelgaard, B., Urtti, A., Moghimi, S.M., Yaghmur, A., 2015. Modulatory effect of human plasma on the internal nanostructure and size characteristics of liquid-crystalline nanocarriers. Langmuir 31, 5042–5049. https://doi.org/10.1021/acs.langmuir.5b00830.
Mousseau, F., Berret, J.F., Oikonomou, E.K., 2019. Design and Applications of a Fluorescent Labeling Technique for Lipid and Surfactant Preformed Vesicles. ACS Omega 4, 10485–10493. https://doi.org/10.1021/acsomega.9b01094.
Mukherjee, A., Waters, A.K., Kalyan, P., Achrol, A.S., Kesari, S., Yenugonda, V.M., 2019. Lipid-polymer hybrid nanoparticles as a nextgeneration drug delivery platform: State of the art, emerging technologies, and perspectives. Int. J. Nanomedicine 14, 1937–1952. https://doi.org/10.2147/IJN.S198353.
Nicola, M., Alsafi, Z., Sohrabi, C., Kerwan, A., Al-Jabir, A., Iosifidis, C., Agha, M., Agha, R., 2020. The socio-economic implications of the coronavirus pandemic (COVID-19): A review. Int. J. Surg. 78, 185–193. https://doi.org/10.1016/j.ijsu.2020.04.018.
Oh, J.Y., Kim, H.S., Palanikumar, L., Go, E.M., Jana, B., Park, S.A., Kim, H.Y., Kim, K., Seo, J.K., Kwak, S.K., Kim, C., Kang, S., Ryu, J.H., 2018. Cloaking nanoparticles with protein corona shield for targeted drug delivery. Nat. Commun. 9, 1–9. https://doi.org/10.1038/s41467-018-06979-4.
Ondicova, K., Tillinger, A., Pecenak, J., Mravec, B., 2019. The vagus nerve role in antidepressants action: Efferent vagal pathways participate in peripheral anti-inflammatory effect of fluoxetine. Neurochem. Int. 125, 47–56. https://doi.org/10.1016/j.neuint.2019.02.003.
Panariti, A., Miserocchi, G., Rivolta, I., 2012. The effect of nanoparticle uptake on cellular behavior: Disrupting or enabling functions? Nanotechnol. Sci. Appl. 5, 87–100. https://doi.org/10.2147/NSA.S25515.
Pardeshi, C.V., Belgamwar, V.S., Tekade, A.R., Surana, S.J., 2013. Novel surface modified polymer-lipid hybrid nanoparticles as intranasal carriers for ropinirole hydrochloride: In vitro, ex vivo and in vivo pharmacodynamic evaluation. J. Mater. Sci. Mater. Med. 24, 2101–2115. https://doi.org/10.1007/s10856-013-4965-7.
Patil, R., Das, S., Stanley, A., Yadav, L., Sudhakar, A., Varma, A.K., 2010. Optimized hydrophobic interactions and hydrogen bonding at the target-ligand interface leads the pathways of drug-designing. PLoS One 5, e12029. https://doi.org/10.1371/journal.pone.0012029.
Pham, V.T., Nguyen, T.Q., Dao, U.P.N., Nguyen, T.T., 2018. On the interaction between fluoxetine and lipid membranes: Effect of the lipid composition. Spectrochim. Acta - Part A Mol. Biomol. Spectrosc. 191, 50–61. https://doi.org/10.1016/j.saa.2017.09.050.

Ravi, P.R., Vats, R., Dalal, V., Gadekar, N., Aditya, N., 2015. Design, optimization and evaluation of poly-ε-caprolactone (PCL) based polymeric nanoparticles for oral delivery of lopinavir. Drug Dev. Ind. Pharm. 41, 131–140. https://doi.org/10.3109/03639045.2013.850710.

Rosen, D.A., Seki, S.M., Fernández-Castañeda, A., Beiter, R.M., Eccles, J.D., Woodfolk, J. A., Gaultier, A., 2019. Modulation of the sigma-1 receptor–IRE1 pathway is beneficial in preclinical models of inflammation and sepsis. Sci. Transl. Med. 11, eaau5266. https://doi.org/10.1126/scitranslmed.aau5266.

Roumestan, C., Michel, A., Bichon, F., Portet, K., Detoc, M., Henriquet, C., Jaffuel, D., Mathieu, M., 2007. Anti-inflammatory properties of desipramine and fluoxetine. Respir. Res. 8, 35. https://doi.org/10.1186/1465-9921-8-35.

Sacre, S., Medghalchi, M., Gregory, B., Brennan, F., Williams, R., 2010. Fluoxetine and citalopram exhibit potent antiinflammatory activity in human and murine models of rheumatoid arthritis and inhibit toll-like receptors. Arthritis Rheum. 62, 683–693. https://doi.org/10.1002/art.27304.

Salatin, S., Barar, J., Barzegar-Jalali, M., Adibkia, K., Kiafar, F., Jelvehgari, M., 2017. Development of a nanoprecipitation method for the entrapment of a very water soluble drug into Eudragit RL nanoparticles. Res. Pharm. Sci. 12, 1–14. https://doi.org/10.4103/1735-5362.199041.

Sanna, V., Roggio, A.M., Pala, N., Marceddu, S., Lubinu, G., Mariani, A., Sechi, M., 2015. Effect of chitosan concentration on PLGA microcapsules for controlled release and stability of resveratrol. Int. J. Biol. Macromol. 72, 531–536. https://doi.org/10.1016/j.ijbiomac.2014.08.053.

Schloer, S., Brunotte, L., Mecate-Zambrano, A., Zheng, S., Tang, J., Ludwig, S., Rescher, U., 2021. Drug synergy of combinatory treatment with remdesivir and the repurposed drugs fluoxetine and itraconazole effectively impairs SARS-CoV-2 infection in vitro. Br. J. Pharmacol. 178, 2339–2350. https://doi.org/10.1111/bph.15418.

Seftel, D., Boulware, D.R., 2021. Prospective Cohort of Fluvoxamine for Early Treatment of Coronavirus Disease 19. Open Forum Infect. Dis. 8, 1–3. https://doi.org/10.1093/ofid/ofab050.

Sengel-Turk, C.T., Hascicek, C., 2017. Design of lipid-polymer hybrid nanoparticles for therapy of BPH: Part I. Formulation optimization using a design of experiment approach. J. Drug Deliv. Sci. Technol. 39, 16–27. https://doi.org/10.1016/j.jddst.2017.02.012.

Shah, V.P., Tsong, Y., Sathe, P., Liu, J.P., 1998. In vitro dissolution profile comparison-Statistics and analysis of the similarity factor, f2. Pharm. Res. 15, 889–896. https://doi.org/10.1023/A:1011976615750.

Silva, M.A.S., Kelmann, R.G., Foppa, T., Cruz, A.P., Bertol, C.D., Sartori, T., Granada, A., Carmignan, F., Murakami, F.S., 2007. Thermoanalyticalstudy of fluoxetine hydrochloride. J. Therm. Anal. Calorim. 87, 463–467. https://doi.org/10.1007/s10973-005-7471-4.

Snipstad, S., Hak, S., Baghirov, H., Sulheim, E., Mørch, Ý., Lélu, S., von Haartman, E., Bäck, M., Nilsson, K.P.R., Klymchenko, A.S., de Lange Davies, C., Åslund, A.K.O., 2017. Labeling nanoparticles: Dye leakage and altered cellular uptake. Cytom. Part A 91, 760–766. https://doi.org/10.1002/cyto.a.22853.

Song, X., Zhao, Y., Hou, S., Xu, F., Zhao, R., He, J., Cai, Z., Li, Y., Chen, Q., 2008. Dual agents loaded PLGA nanoparticles: Systematic study of particle size and drug entrapment efficiency. Eur. J. Pharm. Biopharm. 69, 445–453. https://doi.org/10.1016/j.ejpb.2008.01.013.

Sun, H., Yang, R., Wang, J., Yang, X., Tu, J., Xie, L., Li, C., Lao, Q., Sun, C., 2017. Component-based biocompatibility and safety evaluation of polysorbate 80. RSC Adv. 7, 15127–15138. https://doi.org/10.1039/c6ra27242h.

Tahir, N., Madni, A., Correia, A., Rehman, M., Balasubramanian, V., Khan, M.M., Santos, H.A., 2019. Lipid-polymer hybrid nanoparticles for controlled delivery of hydrophilic and lipophilic doxorubicin for breast cancer therapy. Int. J. Nanomedicine 14, 4961–4974. https://doi.org/10.2147/IJN.S209325.

Thorley, A.J., Ruenraroengsak, P., Potter, T.E., Tetley, T.D., 2014. Critical determinants of uptake and translocation of nanoparticles by the human pulmonary alveolar Epithelium. ACS Nano 8, 11778–11789. https://doi.org/10.1021/nn505399e.

Trezza, A., Iovinelli, D., Santucci, A., Prischi, F., Spiga, O., 2020. An integrated drug repurposing strategy for the rapid identification of potential SARS-CoV-2 viral inhibitors. Sci. Rep. 10, 1–8. https://doi.org/10.1038/s41598-020-70863-9.

Udugama, B., Kadhiresan, P., Kozlowski, H.N., Malekjahani, A., Osborne, M., Li, V.Y.C., Chen, H., Mubareka, S., Gubbay, J.B., Chan, W.C.W., 2020. Diagnosing COVID-19: The Disease and Tools for Detection. ACS Nano 14, 3822–3835. https://doi.org/10.1021/acsnano.0c02624.

Ulferts, R., Van Der Linden, L., Thibaut, H.J., Lanke, K.H.W., Leyssen, P., Coutard, B., De Palma, A.M., Canard, B., Neyts, J., Van Kuppeveld, F.J.M., 2013. Selective serotonin reuptake inhibitor fluoxetine inhibits replication of human enteroviruses B and D by targeting viral protein 2C. Antimicrob. Agents Chemother. 57, 1952–1956. https://doi.org/10.1128/AAC.02084-12.

V'kovski, P., Gerber, M., Kelly, J., Pfaender, S., Ebert, N., Braga Lagache, S., Simillion, C., Portmann, J., Stalder, H., Gaschen, V., Bruggmann, R., Stoffel, M.H., Heller, M., Dijkman, R., Thiel, V., 2019. Determination of host proteins composing the microenvironment of coronavirus replicase complexes by proximity-labeling. Elife 8, 1–30. 10.7554/eLife.42037.

Wang, L., Wang, R., Liu, L., Qiao, D., Baldwin, D.S., Hou, R., 2019. Effects of SSRIs on peripheral inflammatory markers in patients with major depressive disorder: A systematic review and meta-analysis. Brain. Behav. Immun. 79, 24–38. https://doi.org/10.1016/j.bbi.2019.02.021.

WHO, 2017. Stability testing of active pharmaceutical ingredients and finished pharmaceutical products, WHO technical report series.

Wu, D., Wu, T., Liu, Q., Yang, Z., 2020. The SARS-CoV-2 outbreak: What we know. Int. J. Infect. Dis. 94, 44–48. https://doi.org/10.1016/j.ijid.2020.03.004.

Xu, Z., Shi, L., Wang, Y., Zhang, J., Huang, L., Zhang, C., Liu, S., Zhao, P., Liu, H., Zhu, L., Tai, Y., Bai, C., Gao, T., Song, J., Xia, P., Dong, J., Zhao, J., Wang, F.S., 2020. Pathological findings of COVID-19 associated with acute respiratory distress syndrome. Lancet Respir. Med. 8, 420–422. https://doi.org/10.1016/S2213-2600(20)30076-X.

Ye, Q., Wang, B., Mao, J., 2020. The pathogenesis and treatment of the 'Cytokine Storm'' in COVID-19'. J. Infect. 80, 607–613. https://doi.org/10.1016/j.jinf.2020.03.037.

Young, K.C., Bai, C.H., Su, H.C., Tsai, P.J., Pu, C.Y., Liao, C.S., Lin, Y.M., Lai, H.W., Chong, L.W., Tsai, Y.S., Tsao, C.W., 2014. Fluoxetine a novel anti-hepatitis C virus agent via ROS-, JNK-, and PPARβ/γ-dependent pathways. Antiviral Res. 110, 158–167. https://doi.org/10.1016/j.antiviral.2014.08.002.

Yuan, Y., Chiba, P., Cai, T., Callaghan, R., Bai, L., Cole P.C., S., Cai, Y., 2018. Fabrication of psoralen-loaded lipid-polymer hybrid nanoparticles and their reversal effect on drug resistance of cancer cells. Oncol Rep 40, 1055–1063. 10.3892/or.2018.6492.

Zhao, X., Li, F., Li, Y., Wang, H., Ren, H., Chen, J., Nie, G., Hao, J., 2015. Co-delivery of HIF1α siRNA and gemcitabine via biocompatible lipid-polymer hybrid nanoparticles for effective treatment of pancreatic cancer. Biomaterials 46, 13–25. https://doi.org/10.1016/j.biomaterials.2014.12.028.

Zhou, P., Yang, X.-L., Wang, X.-G., Hu, B., Zhang, L., Zhang, W., Si, H.-R., Zhu, Y., Li, B., Huang, C.-L., Chen, H.-D., Chen, J., Luo, Y., Guo, H., Jiang, R.-D., Liu, M.-Q., Chen, Y., Shen, X.-R., Wang, X., Zheng, X.-S., Zhao, K., Chen, Q.-J., Deng, F., Liu, L.-L., Yan, B., Zhan, F.-X., Wang, Y.-Y., Xiao, G.-F., Shi, Z.-L., 2020. A pneumonia outbreak associated with a new coronavirus of probable bat origin. Nature 579, 270–273. https://doi.org/10.1038/s41586-020-2012-7.

Zimniak, M., Kirschner, L., Hilpert, H., Geiger, N., Danov, O., Oberwinkler, H., Steinke, M., Sewald, K., Seibel, J., Bodem, J., 2021. The serotonin reuptake inhibitor Fluoxetine inhibits SARS-CoV-2 in human lung tissue. Sci. Rep. 11, 5890. https://doi.org/10.1038/s41598-021-85049-0.